Atmospheric Water in the Saturated Precipitating Quasi-geostrophic equations

By

Thomas Edwards

A dissertation submitted in partial fulfillment of the

requirements for the degree of

Doctor of Philosophy

(Mathematics)

at the

UNIVERSITY OF WISCONSIN – MADISON

2019

Date of final oral examination: May 7, 2019

The dissertation is approved by the following members of the Final Oral Committee:

Professor N. Chen, Assistant Professor, Mathematics

Professor J. Martin, Professor, Atmospheric and Oceanic Sciences

Professor L. Smith, Professor, Mathematics (Advisor)

Professor S. Stechmann, Professor, Mathematics (Advisor)

Abstract

Water in the atmosphere can exhibit complex phenomena. In this thesis, we investigate some possible behaviors of atmospheric water in the mid-lattitudes. This is done in a saturated setting using the Precipitating Quasi-geopstrophic (PQG) equations. The main results include the following: the scale dependence of atmospheric water on rainfall, the presence and characteristics of Atmospheric Rivers (AR) in PQG, and also the relation between the meridional water flux and rainfall. These results lead to a better understanding of the PQG model in a single phase and also as a precursor for the full PQG model with phase changes.

Acknowledgements

Thank you ... (to be completed later)

Funding for this research was provided by NSF (AGS 1443325, RTG DMS-1147523) and the University of Wisconsin Madison Office of the Vice Chancellor for Research and Graduate Education with funding from the Wisconsin Alumni Research Foundation

List of Figures

List of Tables

Contents

Chapter 1

Introduction

1.1 Introduction

The atmosphere can be challenging to understand not only due to the complex thermodynamic processes, such as phase changes and precipitation processes, but also due to the multi-scale nature of the physical processes, such as rotation and advection. A few historical findings which have advanced the understanding of the atmosphere are the importance of rotation on the winds (Hadley), the equations of motion for fluids (Euler, Navier-Stokes), Kelvin Waves, and more not mentioned here. Some more recent findings are those such as the Quasi-geostrohic theory and baroclinic instability which use a less complicated set of equations compared to the Navier-Stokes equations.

In this thesis, we present some new results from using the Precipitating Quasi-geostrophic (PQG) equations in a saturated environment. These results can be summarized as addressing the spectral slope of water in this set-up, and also the characteristics of Atmospheric Rivers and meridional water fluxes.

Some background material which this thesis incorporates will be mentioned here. The Boussinesq equations, the (dry) Quasi-geostrophic equations, and the Phillips' problem may be familiar to readers of Salmon [1998], Vallis [2006], Pedlosky [2013]. The Fast Auto-conversion and Rain Evaporation (FARE) model as well as the Precipitating-Quasi

Geostrophic (PQG) equations will also be described here.

1.2 Boussinesq Equations

When temperature variations are small within a fluid, the thermodynamic properties of the fluid become essentially constant, and the fluid behaves as approximately an incompressible fluid. However, buoyancy of the fluid is still important as acceleration due to gravity is typically large compared to the acceleration of the fluid [Drazin, 2002].

So that it is easier to compare with equations further on in this chapter, the equations will be written using potential temperature, where it is assumed that potential temperature can be written as a linear background $\theta_0 + \bar{\theta}(z) + \theta$, as is done in Hernandez-Duenas et al. [2013]. The Boussinesq equations can then be written as

$$\frac{\mathrm{D}\mathbf{u}}{\mathrm{D}t} = -\nabla\left(\frac{p}{\rho_0}\right) + g\left(\frac{\theta - \bar{\theta}(z)}{\theta_0}\right)\mathbf{k} \tag{1.1a}$$

$$\nabla \cdot \mathbf{u} = 0 \tag{1.1b}$$

$$\frac{\mathrm{D}\theta}{\mathrm{D}t} = 0 \tag{1.1c}$$

where $\mathbf{u} = (u(\mathbf{x}), v(\mathbf{x}), w(\mathbf{x}))$ is the fluid velocity as a function of three spatial coordinates $\mathbf{x} = (x, y, z)$ and time t; $\theta(\mathbf{x})$ is the anomalous potential temperature from the linearzied base-state $\theta_0 + \bar{\theta}(z)$; and $p(\mathbf{x})$ is pressure. The parameter g is the acceleration due to gravity and ρ_0 is the constant density of the fluid.

1.2.1 Including rotation

To include the effects of rotation on the fluid (more specifically projecting the equation of motion to a coordinate system which is rotating) equation 1.1a would need to include the term $f\mathbf{k} \times \mathbf{u}$ on the left hand side, where f is the Coriolis parameter. When using the $\beta - plane$ approximation $f \approx f_0 + \beta y$.

The equation of motion on a $\beta - plane$ then looks like

$$\frac{\mathrm{D}\mathbf{u}}{\mathrm{D}t} + (f_0 + \beta y)\mathbf{k} \times \mathbf{u} = -\nabla \left(\frac{p}{\rho_0} \right) + g \left(\frac{\theta - \bar{\theta}(z)}{\theta_0} \right) \mathbf{k} \tag{1.2}$$

1.3 Quasi-geostrophic Equations

By taking several assumptions which hold true in the midlatitude atmosphere, the above 6 time-dependent equations can be reduced to one. The assumptions are as follows:

1) The motion of the fluid is nearly geostrophic

$$Ro \ll 1 \tag{1.3}$$

2) The scale of the motion is approximately that of the deformation scale L_d

$$Ro \left(\frac{L}{L_d} \right)^2 = O(Ro) \tag{1.4}$$

3) The changes in the Coriolis parameter are small on the horizontal scale L of the flow

$$\beta L \ll f_0 \tag{1.5}$$

4) Time scales advectively

$$T = L/U \tag{1.6}$$

Using these assumptions and taking the asymptotic limit of $Ro \to 0$ on the non-dimensional Boussinesq equations, the QG equations are obtained:

$$\frac{\mathrm{D}_h PV}{\mathrm{D}t} = 0 \tag{1.7}$$

where

$$PV = \nabla_h^2 \psi + \left(\frac{L}{L_d}\right)^2 \partial_{zz}\psi + \beta y \tag{1.8}$$

where the variables $PV(\mathbf{x}, t), \psi(\mathbf{x}, t)$ are functions of the three dimensions in space $\mathbf{x} = (x, y, z)$ and time t; PV represents potential vorticity and ψ represents the stream-function. The subscript $(\cdot)_h$ indicates that the the operator only has horizontal components (e.g. $\nabla_h = \partial_{xx} + \partial_{yy}$).

1.3.1 Two-level QG and Baroclinic Instability

One of the first mathematical descriptions of baroclinic instability was done by Eady [1949] by solving the linearized QG equations with uniform shear, uniform stratification and also uniform rotation speed ($\beta = 0$). A more complete analysis which allows for $\beta \neq 0$ was done by Charney [1947], however, the analysis is quite complex. By taking a vertical finite difference of the QG equations (see Chapter 2, section 2.2.2 for more details on the derivation), however, a simpler analysis can be done, as was done by Phillips [1951]. This technique has been also used to study moist baroclinic instability (see Appendix A.1.3 for more details and references).

The two level equations with a uniform sheer, $U_1 = U$, $U_2 = -U$ can be written as

$$\frac{\mathrm{D}_1 PV_1}{\mathrm{D}t} - U\partial_x PV_1 + v_1 \partial_y PV_{1,bg} + \beta v_1 = 0 \tag{1.9a}$$

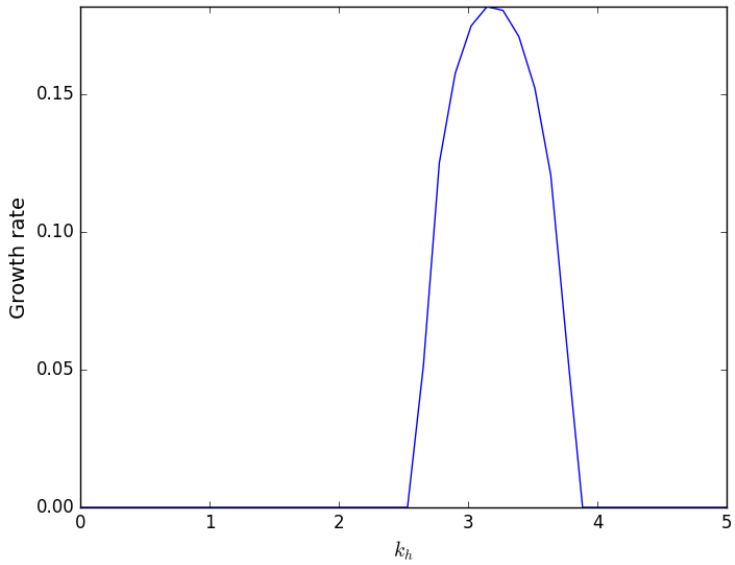

Figure 1: Growth rate of equations 1.9 where $U = 0.2, \beta = 2.5, L/L_d = \sqrt{8}$.

$$\frac{\mathrm{D}_2 PV_2}{\mathrm{D}t} + U\partial_x PV_2 + v_2 \partial_y PV_{2,bg} + \beta v_2 = 0. \tag{1.9b}$$

where $\frac{\mathrm{D}_j(\cdot)}{\mathrm{D}t}$ represents the material derivative with advection by the velocities at level j; $PV_1 = \nabla_h^2 \psi_1 + \left(\frac{1}{\Delta z}\frac{L}{L_d}\right)^2 (\psi_2 - \psi_1)$ the potential vorticity at level 1 and $PV_2 = \nabla_h^2 \psi_2 + \left(\frac{1}{\Delta z}\frac{L}{L_d}\right)^2 (\psi_1 - \psi_2)$ the potential vorticity at level 2; ψ the streamfunction; and L/L_d the ratio of the length scale compared to the deformation radius. (See figure 2 for how the levels are defined.) The background values for PV are represented by $PV_{bg,1}, PV_{bg,2} = -2U(L/(0.5L_{ds}))^2$.

The dispersion relation of the linearized equations from equations 1.9 are shown in the appendix, equation A.3a. Figure 1 is shows the growth rate, when $U = 0.2, \beta = 2.5, L/L_d = \sqrt{8}$. A notable features is that when $\beta = 0$, there is a low-wave number cutoff, such that below this cutoff, the growth rate is zero. Regardless of $\beta = 0$, there will always be a high wave number cutoff.

1.4 Fast Auto-conversion and Rain Evaporation Equations

The Fast Auto-conversion and Rain Evaporation (FARE) equations were originally developed for precipitating convection as equations which contained minimal physics, yet could capture broad features of precipitating turbulent convection [Hernandez-Duenas et al., 2013], compared with cloud resolving models (CRMs) which can more accurately simulate physical processes, but contain much more physical processes which could make it difficult to understand some fundamental features of precipitating convection.

The two main simplifications are: linearized thermodynamics and simplified cloud microphysics. For more details, refer to [Hernandez-Duenas et al., 2013, 2015]

The (dimensional) FARE equations are presented below:

$$\frac{\mathrm{D}\mathbf{u}}{\mathrm{D}t} = -\nabla p + \mathbf{k}g\left[\frac{\theta_e}{\theta_0} + \left(\epsilon_0 - \frac{L_v}{c_p\theta_0}\right)q_v - q_r\right] \tag{1.10a}$$

$$\nabla \cdot \mathbf{u} = 0 \tag{1.10b}$$

$$\frac{\mathrm{D}\theta_e}{\mathrm{D}t} = 0 \tag{1.10c}$$

$$\frac{\mathrm{D}q_t}{\mathrm{D}t} - V_T\frac{\partial q_r}{\partial z} = 0 \tag{1.10d}$$

The variables θ_e, q_t, q_r, q_v represent equivalent potential temperature, the mixing ratio of total rain, rain water, and water vapor respectively. The parameters L_v, c_p, V_T represent the latent heat factor, the specific heat, and the rainfall speed. The parameter ϵ_0 is related to the ratio of gas constants by $\epsilon_0 = 1 - R_v/R_d$.

1.5 Precipitating Quasi-geostrophic Equations

There have been numerous studies which include moisture or moisture effects in a QG setting. These have provided insight into the dynamics of moisture and the role of latent heat release in atmosphere. To name a few examples, Mak [1982], Bannon [1986] investigated baroclinic instability with condensational heating using a similar approach in the Eady problem; Lapeyre and Held [2004] observed that the effective static stability could be reduced with moisture and latent heat release. An unusual feature of the PQG equations is that these equations are asymptotic limiting equations.

Similar to how the dry QG equations were derived, by taking an asymptotic limit of the FARE equations with $Ro \to 0$, and similar assumptions on the deformation radius, the Precipitating Quasi-geostrophic equations can be obtained. Refer to Smith and Stechmann [2017], Wetzel et al. [2017] and also chapter 2 of this text for more details.

Chapter 2

Atmospheric Water Scaling

2.1 Introduction

Atmospheric water is notoriously difficult to model, predict, and understand. This is in part due to the multitude of physical processes involved in the dynamics of water, such as precipitation and related processes.

The power spectrum of water—i.e., the scale dependence of its variance—seems to reflect water's complex physics and dynamics. In particular, a range of spectral exponents has been reported in observations of water, as widely as a range of -1.3 to -2.7, but more commonly in terms of convenient numbers as a range of $-5/3$ to -2 [Nastrom et al., 1986, Cho et al., 2000, Kahn and Teixeira, 2009, Kahn et al., 2011, Fischer et al., 2012, Pressel and Collins, 2012]. A variety of factors could influence the spectrum of water, such as, e.g., precipitation and meridional and vertical gradients of the background state, and by investigating the influence of different factors, a better understanding of the physics and dynamics of water could be obtained.

In this chapter, the overarching question is: Can some theoretical insight be gained for the spectrum of water? To carry out the investigation here, a quasi-geostrophic (QG) framework is used owing to its simplicity and amenability to theoretical understanding. In the past, for instance, some of the achievements of the QG equations include, but

are not limited to, explaining baroclinic instability [Charney, 1947, 1948, Phillips, 1954] and geostrophic turbulence [Rhines, 1979, Salmon, 1980]. With such a background, it is reasonable to hope that further understanding of water can be achieved in a similar framework. Here it is shown that, in a simple moist QG framework, the spectral exponent of water can take a range of values, and the spectrum can change significantly due to the influence of precipitation.

As a quasi-geostrophic model with water, the recently derived precipitating quasi-geostrophic (PQG) equations will be used [Smith and Stechmann, 2017]. For comparison, there have been other variations/adaptations of the dry QG equations to include moisture and moisture effects via latent heat release, etc. [e.g., Mak, 1982, Bannon, 1986, Lapeyre and Held, 2004, Monteiro and Sukhatme, 2016]; these and other similar models [e.g., Lambaerts et al., 2012] have provided insight into moisture dynamics and the role of latent heat release in the atmosphere. One distinguishing and advantageous property of the PQG equations is that they are asymptotic limiting equations. Specifically, the PQG equations arise in the limit of rapid rotation and strong (moist) stratification, starting from the equations for midlatitude dynamics with moisture, phase changes, and precipitation [Hernandez-Duenas et al., 2013].

The ideas of passive versus active tracers will play an important role in providing theoretical understanding. In particular, theoretical analysis is made possible here by the observation that the model total water can be written as a linear combination, as $q_t = M - G_M\theta_e$, of a passive tracer M and an active tracer θ_e. These two quantities are each related to an eigenmode of the system: M is related to a moist eigenmode that is not present for a dry system, and θ_e is the equivalent potential temperature and is related to the vortical mode. By understanding the individual spectra of the

passive and active tracers, the spectrum of total water can then be better understood. For instance, differences in spectra due to a variable behaving as a passive tracer or an active tracer have been observed in other previous studies, for example in Babiano et al. [1987], Lapeyre et al. [2001], Smith et al. [2002], and such results aid the theoretical analysis here. It may seem counterintuitive that ideas of active tracers are used here to understand the spectrum of water, since in the present setup the underlying dynamics of velocity can be determined without consideration of the dynamics of the water variable; such a lack of feedback seems to suggest that the water is a passive tracer in this setup. Nevertheless, it is also true that the water can be written as a linear combination, $q_t = M - G_M \theta_e$, of a passive tracer M and an active tracer θ_e, which suggests that water could possibly be viewed as an active tracer in some sense, or at least that ideas related to active tracers could be used to provide a better understanding of water.

It is worth noting some of the complicating factors that are either neglected here, or are not accessible within the framework of this chapter. As one example, phase changes of water will be neglected here in order to facilitate some theoretical analysis. While phase changes of water are undoubtedly important, it is possible to include some aspects of precipitation without including the nonlinear switch associated with phase changes, and it allows some theoretical understanding. As another example, the use of a quasi-geostrophic model implies an assumption of dynamics that are large-scale (synoptic-scale) and extratropical, whereas some of the observational studies listed in an earlier paragraph were associated with smaller-scale behavior of water and convection, and not necessarily outside the tropics. For instance, Cho et al. [2000] report measurements from the tropics and also from the extratropics, and Fischer et al. [2012] and Cho et al. [2000] use aircraft data that describes length scales of 100 km and smaller, whereas other

studies such as Kahn and Teixeira [2009] report satellite observations for length scales of ∼150 to 1300 km. As a third example, the model here will use a crude vertical structure, whereas the observational studies mentioned earlier were taken from a variety of vertical levels in the atmosphere; for instance, Cho et al. [2000] observed a spectral slope of -1.46 in the boundary layer and a slope of -1.79 in the extratropical free troposphere; Kahn et al. [2011] observed an increase in slope with height from -1.58 at 1.5 km height to -1.90 at 3 km; and in their LIDAR study, Fischer et al. [2012] observed -1.29 at lower altitudes and -2.68 at higher altitudes. Other studies have used more comprehensive versions of the dynamics [Spyksma and Bartello, 2008, Sukhatme et al., 2012, Schemann et al., 2013, Mellado, 2017], without neglecting some or all of the factors listed above, and are therefore able to provide a more precise connection to observational data, but at the expense of complicating the possibility of a theoretical analysis like the one considered here. For instance, the theoretical analysis here uses the linear decomposition of $q_t = M - G_M\theta_e$ to write q_t as a sum of a passive tracer M and an active tracer θ_e, and such a decomposition would become nonlinear (piecewise linear) in the presence of phase changes.

The organization of the chapter is as follows. In section 2, the precipitating quasi-geostrophic (PQG) model is described, as well as details of the numerical method used to solve the system projected onto two vertical levels. In section 3, the results from the numerical simulations of 2-level PQG are presented. In section 4, a theoretical explanation is provided for the exponent of the water spectra from the previous simulations. In section 5, the effect of adding a meridional gradient to water is investigated, and the discussion and conclusion are in section 6.

2.2 PQG Model Description

The PQG equations can be considered as a moist version of the QG equations. The dry QG equations describe the slow evolution of synoptic-scale flows under assumptions of rapid rotation and strong stratification. Derivations for the dry QG equations can be found in Salmon [1998], Vallis [2006], Pedlosky [2013].

PQG is derived starting from a cloud resolving model. Conversions between water vapor, cloud water and rain water are modeled at macroscopic scales, and each conversion process is associated with a time scale. For evolution of mid-latitude flows on length scales of kilometers and time scales of hours to days, the time scales for conversions of water substance are relatively short, on the order of seconds to minutes, compared to the characteristic times associated with rotation, buoyancy effects, advection and rainfall [Rogers and Yau, 1989, Houze, 1993, Klein and Majda, 2006, Morrison and Grabowski, 2008]. Thus, for large-scale mid-latitude flows, the assumption of asymptotically fast cloud microphysics leads to a particularly simple model description denoted FARE, standing for the assumptions of 'fast auto-conversion and rain evaporation,' in addition to fast condensation [Hernandez-Duenas et al., 2013]. Beyond the assumptions of the dry QG framework (rapid rotation and strong dry stratification), an additional assumption in the PQG framework is a strong moist stratification of equivalent potential temperature [Smith and Stechmann, 2017, Wetzel et al., 2017]. Furthermore, in PQG, boundaries between unsaturated and saturated flow regions are represented by Heaviside nonlinear switches: water below the saturation level exists in the vapor phase only; water above the saturation level is instantaneously converted to rain water, which falls at a constant speed V_r.

Table 1: Definition of variables

$\mathbf{x} = (x, y, z)$	Horizontal coordinates
t	Time
$\mathbf{u}(\mathbf{x}, t) = (u, v, w)$	Velocities
$\mathbf{u}_h = (u, v)$	Horizontal velocities
$\zeta(\mathbf{x}, t) = \partial_x v - \partial_y u$	Relative vorticity
$\psi(\mathbf{x}, t)$	Streamfunction (pressure scaled by constant density)
θ	Potential temperature
$q_v(\mathbf{x}, t)$	Water vapor mixing ratio
$q_r(\mathbf{x}, t)$	Rain water mixing ratio
$q_t(\mathbf{x}, t) = q_v + q_r$	Total water mixing ratio
$\theta_e(\mathbf{x}, t) = \theta + q_v$	Equivalent potential temperature
$PV(\mathbf{x}, t) = \nabla_h^2 \psi + (L/L_{ds})^2(\partial^2\psi/\partial z^2)$	Potential Vorticity
$M(\mathbf{x}, t) = q_t + G_M \theta_e$	Thermodynamic variable M

Table 2: Dimensional parameters and typical values

L	1000km	Characteristic length scale
L_{ds}	700km	Saturated deformation
c_p	10^3 J kg^{-1} K^{-1}	Specific heat
L_v	2.5×10^6 J	Latent heat factor
$\mathrm{d}\tilde{\theta}_e/\mathrm{d}z$	1.5 K km^{-1}	Background vertical gradient of equivalent potential temperature
$\mathrm{d}\tilde{q}_t/\mathrm{d}z$	-0.6 g kg^{-1} km^{-1}	Background vertical gradient of rain water
V_T	$0.3 - 10$ m s^{-1}	Rainfall speed
U_0	10 m s^{-1}	Characteristic mid-latitude horizontal velocity
W_0	0.1 m s^{-1}	Characteristic vertical velocity
β_0	2.5×10^{-11} m^{-1} s^{-1}	Change in rate of rotation

Here we focus on the structure and statistics of water, and for simplicity consider exclusively saturated domains. After introducing the continuously stratified PQG equations in a saturated environment in section 2.1, the 2-level PQG equations and boundary conditions are described in detail in section 2.2. Next, we provide an overview of the numerical method and the model parameters used for our 2-level PQG simulations in section 2.3. We end the section with descriptions of the basic structures of the dry and moist variables in section 2.4.

Table 3: Nondimensional parameters

L/L_{ds}	Nondimensional ratio of length scales
$\beta = L^2\beta_0/U_0$	Nondimensional change in rate of rotation
$G_M = -L_v c_p^{-1}(\mathrm{d}\tilde{q}_t/\mathrm{d}z)\,(\mathrm{d}\tilde{\theta}_e/\mathrm{d}z)^{-1}$	Ratio of the background vertical gradients of q_t and θ_e
$V_r = V_T/W_0$	Nondimensional rainfall speed

Table 4: Notation for derivatives

$\frac{\mathrm{D}}{\mathrm{D}t} = \partial_t + \mathbf{u}\cdot\nabla_h$	Material derivative
$\nabla_h = \hat{\mathbf{x}}\,\partial_x + \hat{\mathbf{y}}\,\partial_y$	Horizontal laplacian
$\frac{\mathrm{D}_h}{\mathrm{D}t} = \partial_t + \mathbf{u}_h\cdot\nabla_h$	Horizontal material derivative

2.2.1 PQG equations

Including the variation of the Coriolis parameter with latitude (the β-effect; see e.g., Vallis [2006]), the PQG equations may be written in nondimensional form by

$$\frac{\mathrm{D}_h\zeta}{\mathrm{D}t} + \beta v = \frac{\partial w}{\partial z} \tag{2.1a}$$

$$\frac{\mathrm{D}_h\theta_e}{\mathrm{D}t} + \frac{L_{ds}}{L}w = 0 \tag{2.1b}$$

$$\frac{\mathrm{D}_h q_t}{\mathrm{D}t} - G_M\frac{L_{ds}}{L}w = V_r\frac{\partial q_r}{\partial z} \tag{2.1c}$$

where the variables $\mathbf{u}(\mathbf{x},t), \zeta(\mathbf{x},t), \theta_e(\mathbf{x},t), q_t(\mathbf{x},t), q_r(\mathbf{x},t)$ are functions of three space dimensions $\mathbf{x} = (x,y,z)$ and time t; $\mathbf{u} = (u,v,w)$ is the fluid velocity with horizontal components $\mathbf{u}_h = (u,v)$; $\zeta = \partial_x v - \partial_y u$ is the vertical component of relative vorticity; θ_e is the equivalent potential temperature; q_t is the mixing ratio of total water; and q_r is the mixing ratio of rain water. With linearized thermodynamics, $\theta_e = \theta + q_v$, where $\theta(\mathbf{x},t)$ is the potential temperature and $q_v(\mathbf{x},t)$ is the mixing ratio of water vapor. The

Table 5: Notation of variable location

$(\cdot)_1$	$(\cdot)$ at level 1
$(\cdot)_2$	$(\cdot)$ at level 2
$(\cdot)_m$	$(\cdot)$ at the mid-domain (between level 1 and level 2)

horizontal material derivative $\frac{\mathrm{D}_h}{\mathrm{D}t} = \partial_t + \mathbf{u}_h \cdot \nabla_h$, where $\nabla_h = \hat{\mathbf{x}}\,\partial_x + \hat{\mathbf{y}}\,\partial_y$, appears instead of the full material derivative $\frac{\mathrm{D}}{\mathrm{D}t} = \partial_t + \mathbf{u} \cdot \nabla$, as discussed below. Summaries of the variables, parameters, and symbols are provided in Tables 1–4.

The velocity and vorticity are anomalous quantities assuming a Boussinesq background state of rest, whereas all thermodynamic quantities have been decomposed into Boussinesq background functions of altitude and anomalies; for example, the total equivalent potential temperature $\theta_e^{tot}(\mathbf{x}, t) = \tilde{\theta}_e(z) + \theta_e(\mathbf{x}, t)$ and the total water $q_t^{tot}(\mathbf{x}, t) = \tilde{q}_t(z) + q_t(\mathbf{x}, t)$. In this Boussinesq setting, the background gradients $d\tilde{\theta}_e/dz$ and $d\tilde{q}_t/dz$ are taken to be constants. Also, $\tilde{q}_r$ is chosen to be a constant so that $d\tilde{q}_r/dz = 0$ and the background states $\tilde{(\cdot)}$ are a steady state solution of (2.1). As a result, since $\tilde{q}_t = \tilde{q}_v + \tilde{q}_r = \tilde{q}_{vs} + \tilde{q}_r$, the gradients $d\tilde{q}_t/dz$ and $d\tilde{q}_{vs}/dz$ are equal in this setup and the anomalous total water, q_t is equal to the anomalous rain water, q_r. (See appendix 7.1 for more details.) In the saturated setup here, upward motion is always associated with condensation and latent heating, and downward motion is always associated with evaporation and evaporative cooling. While the environmental background state is chosen to be saturated here, it could also be chosen to be unsaturated in the more general case [Smith and Stechmann, 2017].

Underlying the saturated PQG system (2.1) are the geostrophic and hydrostatic balances, resulting from, respectively, fast rotation and strong stable stratification:

$$\hat{\mathbf{z}} \times \mathbf{u} = -\nabla_h \psi \tag{2.2a}$$

$$\theta_e = \frac{L}{L_{ds}} \frac{\partial \psi}{\partial z}, \tag{2.2b}$$

where ψ is a streamfunction (pressure scaled by the constant density). Note that the buoyancy in (2.2b) depends on θ_e but does not include the dependence on water vapor

and liquid water, such as water loading, that is typical of the Boussinesq and anelastic equations; this latter dependence is not included here because these effects are asymptotically small in the precipitating quasi-geostrophic limit [see Smith and Stechmann, 2017, for more details]. The balances (2.2) may be used to rewrite the PQG equations (2.1) in terms of the streamfunction ψ in place of u, v, ζ, θ_e, with $\zeta = \nabla_h^2 \psi$. The geostrophic-hydrostatic balances (2.2) constrain the vertical velocity w to be small compared to the horizontal velocity $\mathbf{u}_h$, leading to dominance of horizontal advection reflected by the operator $\frac{\mathrm{D}_h}{\mathrm{D}t} = \partial_t + \mathbf{u}_h \cdot \nabla_h$. Equations (2.1a), (2.1b) and (2.2) are mathematically equivalent to the dry quasi-geostrophic equations after replacing the saturated deformation radius L_{ds} by the dry deformation radius L_d [Salmon, 1980, Vallis, 2006, Pedlosky, 2013].

In equations 2.1, there are four nondimensional parameters in the PQG equations: the length-scale ratio L_{ds}/L; change in the rotation rate with latitude, β; the rainfall speed, V_r; and the scaled ratio of the background vertical gradients of total water and equivalent potential temperature, G_M. Later on in section 5, a fifth nondimensional parameter, the meridional gradient of water, Q_y is considered. Tables 2–3 list the dimensional and nondimensional parameters and relationships between them.

Periodic boundary conditions are imposed in the horizontal directions, and a rigid lid boundary condition $w = 0$ is imposed at top and bottom. Applying these boundary condition to equations (2.1)-(2.2), the vertical boundary condition becomes

$$w = 0, \quad \frac{\mathrm{D}_h \theta_e}{\mathrm{D}t} = 0, \quad \frac{\mathrm{D}_h q_t}{\mathrm{D}t} = V_r \frac{\partial q_r}{\partial z} \tag{2.3}$$

on both top and bottom. Further boundary conditions on q_r will also be specified such as no inflow of q_r and this is discussed further in the description of the two-level setup

in section 2.2.2.

In what follows, we recall from the discussion between (2.1) and (2.2) that the current setup is fully saturated, so the anomaly q_r represents the same quantity as q_t:

$$q_r = q_t. \tag{2.4}$$

From here on, all q_r values will be replaced with q_t.

Following a similar procedure as for dry QG, the vertical velocity w may be eliminated from (2.1) by introducing the potential vorticity PV and a thermodynamic variable M:

$$PV = \nabla_h^2 \psi + \left(\frac{L}{L_{ds}}\right)^2 \frac{\partial^2 \psi}{\partial z^2} \tag{2.5a}$$

$$M = q_t + G_M \theta_e \tag{2.5b}$$

leading to the dynamical equations

$$\frac{\mathrm{D}_h PV}{\mathrm{D}t} + \beta v = 0 \tag{2.6a}$$

$$\frac{\mathrm{D}_h M}{\mathrm{D}t} = V_r \frac{\partial}{\partial z} q_t. \tag{2.6b}$$

For the PQG system, there are coupled equations (2.6) for PV and M, the latter which is simply the combination of (2.1b) and (2.1c) that eliminates w within this framework.

2.2.2 Two-level PQG

There are several derivations of the dry two level QG equations, such as in Phillips [1954], Salmon [1998]. Here we include a detailed derivation of PQG to make clear how the discretized equation for M is obtained, and how we implement boundary conditions for q_t and M.

According to the two-level set-up shown in figure 2, we use the notation $\frac{\mathrm{D}_1}{\mathrm{D}t}(\cdot) = \partial_t(\cdot) + u_1\partial_x(\cdot) + v_1\partial_y(\cdot)$, and similarly for $\frac{\mathrm{D}_2}{\mathrm{D}t}(\cdot)$ and $\frac{\mathrm{D}_m}{\mathrm{D}t}(\cdot)$. Using a finite difference approximation in z of (2.6) and specific initial/boundary conditions described below, we arrive at the two level PQG equations given by

$$\frac{\mathrm{D}_1 PV_1}{\mathrm{D}t} + \beta v_1 = 0 \tag{2.7a}$$

$$\frac{\mathrm{D}_2 PV_2}{\mathrm{D}t} + \beta v_2 = 0 \tag{2.7b}$$

$$\frac{\mathrm{D}_m M_m}{\mathrm{D}t} = -\frac{V_r}{\Delta z} q_{t,m} = -\frac{V_r}{\Delta z}(M_m - G_M \theta_{e,m}) \tag{2.7c}$$

with

$$PV_1 = \nabla_h^2 \psi_1 + \left(\frac{1}{\Delta z}\frac{L}{L_{ds}}\right)^2 (\psi_2 - \psi_1) \tag{2.8a}$$

$$PV_2 = \nabla_h^2 \psi_2 + \left(\frac{1}{\Delta z}\frac{L}{L_{ds}}\right)^2 (\psi_1 - \psi_2) \tag{2.8b}$$

$$\theta_{e,m} = \frac{L}{L_{ds}}\frac{\psi_2 - \psi_1}{\Delta z} \tag{2.8c}$$

$$u_i = -\frac{\partial \psi_i}{\partial y} \text{ for } i = 1, 2 \tag{2.8d}$$

$$v_i = \frac{\partial \psi_i}{\partial x} \text{ for } i = 1, 2 \tag{2.8e}$$

$$u_m = \frac{u_1 + u_2}{2} \tag{2.8f}$$

$$v_m = \frac{v_1 + v_2}{2}. \tag{2.8g}$$

In quasigeostrophic literature, the velocities u_m, v_m are also known as the barotropic (depth-averaged) velocities. Expressions (3.3a)-(3.3c) are obtained by a centered difference in z of (2.6a) with $\frac{1}{\Delta z}\left(\frac{\partial \psi}{\partial z}|_{z=z_m} - \frac{\partial \psi}{\partial z}|_{z_B}\right)$ for level 1, and $\frac{\partial^2 \psi}{\partial z} \approx \frac{1}{\Delta z}\left(\frac{\partial \psi}{\partial z}|_{z_T} - \frac{\partial \psi}{\partial z}|_{z=z_m}\right)$ for level 2, and where z_B, z_m, z_T denote z at the bottom, middle and top, respectively. For an initial condition of $\theta_e = 0$ at top and bottom, the second equation of (2.3) ensures

Figure 2: Diagram of the two-level set-up. The variables q_t, M, θ_e are in fact $q_{t,m}, M_m, \theta_{e,m}$, the indices were dropped here so as to match the variables in the later sections.

that the value will remain zero for all time, and hence that $\frac{\partial \psi}{\partial z}|_{z_T} = \frac{\partial \psi}{\partial z}|_{z_B} = 0$ for all time by (2.2b). For the more general vertical boundary condition $\frac{\mathrm{D}_h \theta_e}{\mathrm{D}t} = 0$, it was shown that the interior two-level dry QG equations are unchanged [Phillips, 1954, Salmon, 1998]. The same result also holds for the 2-level PQG equations within a single phase, either unsaturated or saturated, but not in an environment with phase changes. For simplicity, and since we consider a domain that is completely saturated for all time, we use the vertical boundary condition $\theta_e = 0$ as done similarly in the dry QG case (e.g. in Held and O'Brien [1992]).

To obtain (3.2c), an upwind difference was taken to approximate (2.6b). For example at z_m, $\frac{\partial}{\partial z}\left(M - G_M \theta_e\right)|_{z=z_m} \approx \frac{V_r}{\Delta z}\left(q_t|_{z=z_T} - q_t|_{z=z_m}\right)$. Imposing the initial condition that $q_t(t=0) = 0$ for $z \geq z_T$, the upwind approximation of the third equation in (2.3) gives $q_t(z = z_T) = 0$ for all time. From this latter condition, $\frac{\partial}{\partial z}\left(M - G_M \theta_e\right)|_{z=z_m} \approx \frac{V_r}{\Delta z}\left(0 - \left(M_m - G_M \theta_{e,m}\right)\right)$. Since the main interest is on the dynamics of the moist variables in the interior (M_m and $q_{t,m}$), and because the moist variables at the lower boundary do not affect the values of the moist variables in the interior, the M-equation at the lower boundary is omitted. To simplify notation, the subscript m will be dropped from θ_e, M from here on.

2.2.3 Discretized model for numerical computations

Our main goal is to investigate the structure and statistics of water in a statistically quasi-steady state of saturated PQG, evolving from baroclinically unstable initial conditions. To this end, we numerically computed the solution to (3.2) with additional dissipation terms given by 4th-order hyperviscosity and lower-level friction:

$$\frac{\mathrm{D}_1 PV_1}{\mathrm{D}t} - U\partial_x PV_1 + v_1 \partial_y PV_{1,bg} + \beta v_1 = -\kappa_M \Delta \psi_1 - \nu \Delta^4 PV_1 \tag{2.9a}$$

$$\frac{\mathrm{D}_2 PV_2}{\mathrm{D}t} + U\partial_x PV_2 + v_2 \partial_y PV_{2,bg} + \beta v_2 = -\nu \Delta^4 PV_2 \tag{2.9b}$$

$$\frac{\mathrm{D}_m M}{\mathrm{D}t} + v_m \partial_y M_{bg} = -\frac{V_r}{\Delta z}\left(M - G_M \theta_e\right) - \nu \Delta^4 M. \tag{2.9c}$$

The parameter values $U = 0.2$, $\beta = 2.5$, $\kappa_M = 0.05$, $\nu = 5 \times 10^{-15}$ and $k_{ds} = 4$ were chosen to match the (dry) mid-latitude atmosphere case studied in Qi and Majda [2016]. The expressions for the background values of θ_e and PV are, respectively, $\theta_{e,bg} = \Theta y = -\frac{L}{L_{ds}}\frac{1}{\Delta z}(2Uy)$ and $PV_{j,bg} = (-1)^j \left(\frac{1}{\Delta z}\frac{L}{L_{ds}}\right)^2 (2Uy)$. The parameters reflecting the presence of water in our 2-level PQG equations are G_M and V_r: G_M depends on the background water profile and V_r is the rainfall speed. In the present study, we fix the value $G_M = 1$ and vary V_r. The baseline case considered in Sections 2.3 and 2.4 has background meridional gradient $Q_y = 0$ such that $M_{bg} = (Q_y + G_M\Theta)y = G_M \Theta y$; $Q_y \neq 0$, $G_M \neq 1$ is considered in Section 2.5.

A pseudospectral solver was used to solve (3.4) on a doubly periodic, horizontal domain. The time-stepping was done according to a 3rd-order Runge-Kutta scheme with an adaptive Δt chosen to satisfy the CFL condition. Three-halfs padding was used for de-aliasing. Most of the simulations used resolution $N^2 = 512^2$ Fourier modes, with a few higher-resolution simulations as described below. The initial condition was

a band of eigenmodes centered around the unstable wave-vector $(k, l) = (3, 1)$, and the simulations were run long enough to obtain statistical steady states. These eigenmodes can be obtained by solving the linearized equation (see appendix for more details on the linearized equations and initial condition setup). In addition to the two modes obtained from the PV equations, as done in dry QG, there is another eigenmode from the M equation that is not present in dry QG.

2.2.4 Basic structure of the statistical steady state (baseline case)

We end this section with figure 3 of zonally averaged variables in a time interval $t \in [60, 100]$, in part to demonstrate that the chosen parameter values for β, deformation radius k_{ds}^{-1}, and background vertical shear U are consistent with mid-latitude dynamics. Zonal averages are denoted by an overbar, e.g., the zonally averaged zonal velocity at mid-height is denoted $\bar{u}_m(t, y)$. Figure 3 will also help with interpretation of later single-time plots visualizing the water variables q_t and $M = q_t + G_M\theta_e$ in the (x, y)-plane.

Figure 3a shows a single, persistent, eastward jet with minimal meandering in this relatively short time window; some meandering is observed for longer time windows as for the mid-latitude case of Qi and Majda [2016]. The asymmetry in the jet, with the westward jet being broader and the eastward jet being narrower, is related to the β effect [e.g., Kuo, 1949, Armi, 1989]. The potential temperature shown in figure 3b is approximately constant below and above the jet, which separates warm air to the south from colder air to the north. There is a gradient of decreasing temperature across the jet region. Within the saturated one-phase PQG approximation, the dynamics of

ψ, and hence the dynamics of velocity $\mathbf{u}$ and temperature θ_e, are not changed by the presence of water. Thus figures 3a and 3b are the same for all values of rainfall speed V_r. However, the dynamics of the water variables q_t and M depend crucially on V_r as will be demonstrated in the following Sections. For $V_r = 0.1$, the large-scale features of $\bar{M}(t, y)$ roughly mirror the features of $\bar{\theta}_e(t, y)$, but with more fine-scale structure (figure 3c). The zonally averaged anomalous water q_t is concentrated at the boundaries of the jet, with less water on the southern warm side and more water on the northern cold side (figure 3d). A more detailed analysis of zonally averaged water and meridional water fluxes is planned for a forthcoming manuscript.

To view the simulations from a PV perspective, the power spectra for PV_1, PV_2 and kinetic energy at level 1,2 as well as the potential energy are presented in figure 4b. The simulations for this chapter are in the forward enstrophy cascade regime, with the KE spectra matching those found in Qi and Majda [2016], also in the forward cascade regime. If simulations were run in a different regime, a regime with the inverse cascade, one would expect a different shape, notably a flatter KE spectra with a -5/3 slope, such as those found in [Larichev and Held, 1995, Smith and Vallis, 2001].

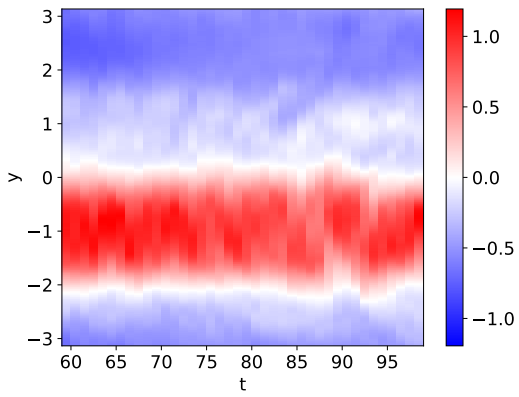

(a) $\bar{u}_m(t, y)$

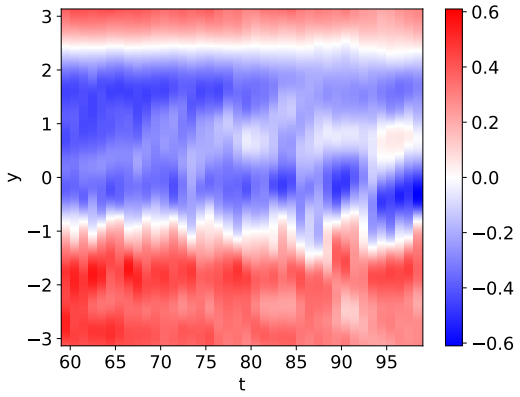

(b) $\bar{\theta}_e(t, y)$

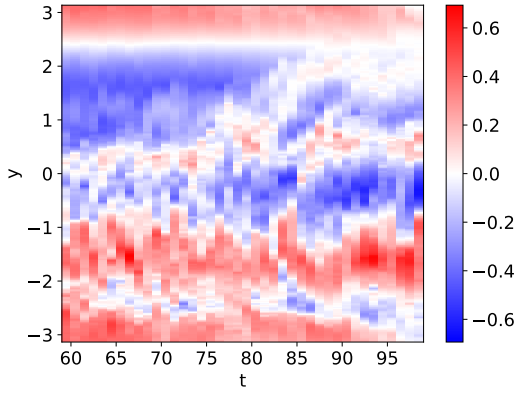

(c) $\bar{M}(t, y)$ for $V_r = 0.1$

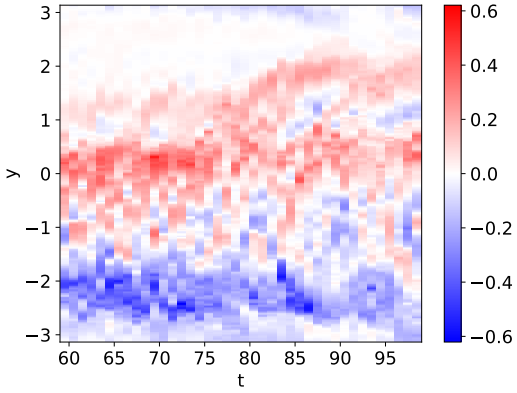

(d) $\bar{q}_t(t, y)$ for $V_r = 0.1$

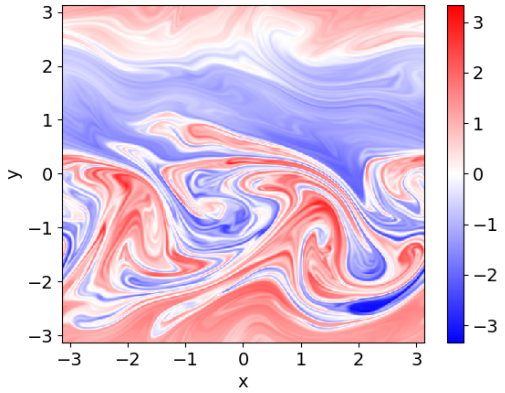

(e) Snapshot of PV_1

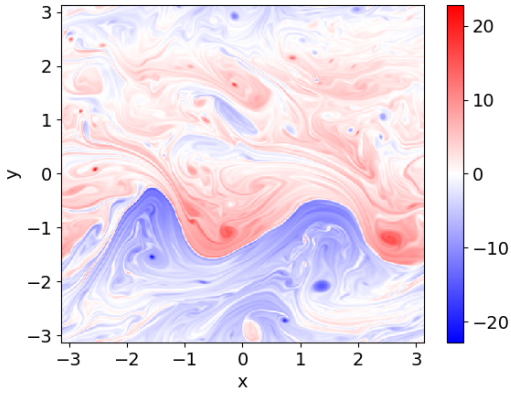

(f) Snapshot of PV_2

Figure 3: Panels (a)-(d) show zonally averaged quantities as a function of time t and meridional direction y: (a) zonal velocity $\bar{u}_m$, (b) equivalent potential temperature $\bar{\theta}_e$, (c) $\bar{M}(t, y)$ for $V_r = 0.1$, (d) total water $\bar{q}_t$ for $V_r = 0.1$, and (e) snapshot of PV_1 at $t = 60$ (f) snapshot of PV_2 at $t = 60$. One time unit corresponds to about one day.

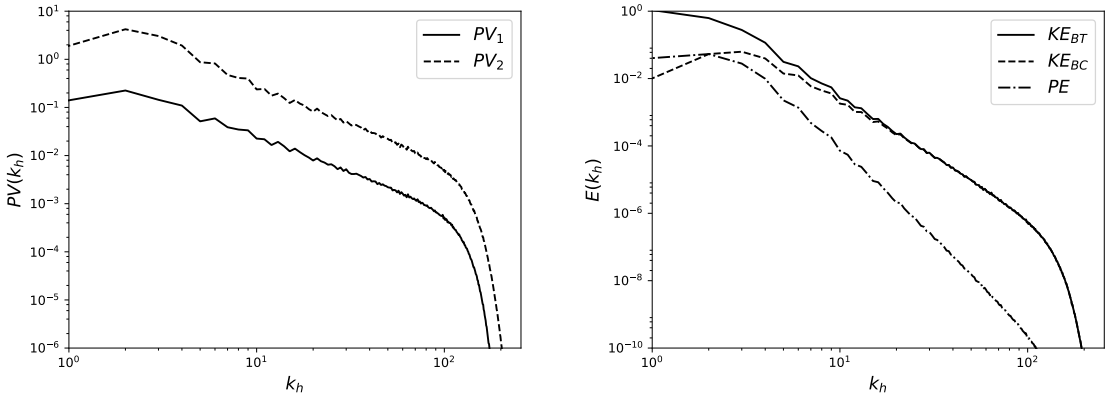

(a) Spectra of PV_1, PV_2

(b) Spectra of KE_1, KE_2, PE

Figure 4: Panels (a), (b) show the spectra of (a) PV_1, PV_2 and (b) Kinetic Energy at level 1, KE_1 and level 2, KE_2 and Potential Energy, PE.

2.3 Simulation results for water variables

In this section, the variability of water is investigated, and it is illustrated in terms of both its physical-space structure (section 2.3.1) and its power spectral density (section 2.3.2). A main goal is to explore how the water variability changes (if at all) as the precipitation changes, as controlled in the model here by the parameter V_r.

2.3.1 Physical-space structure

Single-time snapshots of anomalous water q_t and $M = q_t + G_M \theta_e$ are shown in figure 5, where the different rows correspond to different values of rainfall speed $V_r = 0, 0.1, 1.0$. The time is $t = 60$, after the simulation has reached a statistically steady state, and the height is mid-level between levels 1 and 2 (see figures 2 and 3). One can see that both the amplitude and variability of water depend strongly on V_r, with both amplitude and fine-scale structure decreasing as V_r increases, similar to dissipation without scale-selectivity. For $V_r = 0$, q_t is indistinguishable to the eye from M. By contrast, for the large value of $V_r = 10$ in figure 6, q_t is seen to inherit the structure of vertical velocity w, while M is indistinguishable to the eye from θ_e.

From the q_t plots in both figures 5-6, one anticipates that variance spectra for water q_t will steepen as rainfall speed V_r increases and fine-scale structure decreases. In the next section 2.3.2, we quantify the range of spectral scalings and the limiting spectral exponents for $V_r \to 0$ and $V_r \to \infty$. Later in section 2.4, we provide a rational basis for understanding the structural transition from $q_t \sim M$ for $V_r \to 0$, to $q_t \sim w$ for $V_r \to \infty$.

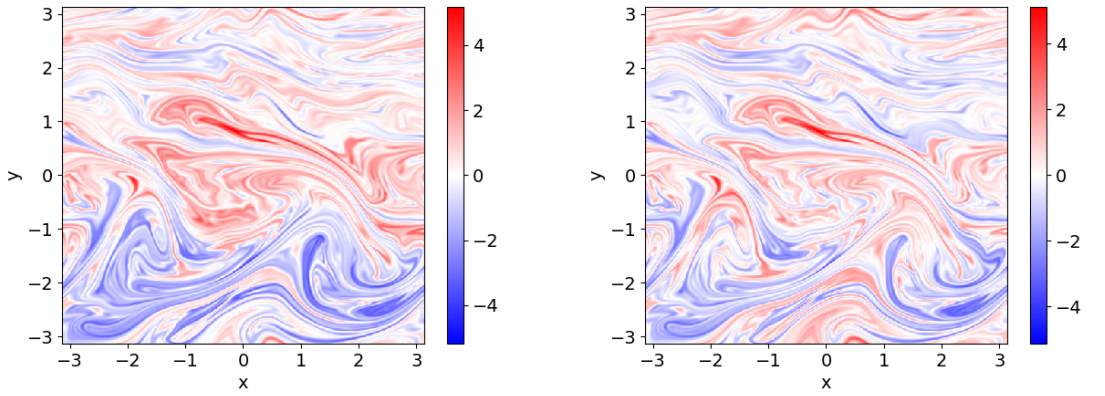

(a) q_t, $V_r = 0$ (b) M, $V_r = 0$

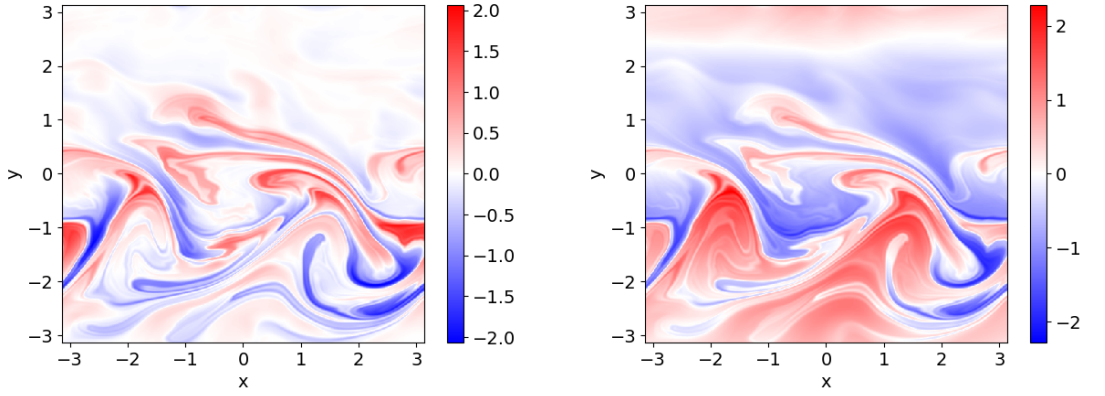

(c) q_t, $V_r = 0.1$ (d) M, $V_r = 0.1$

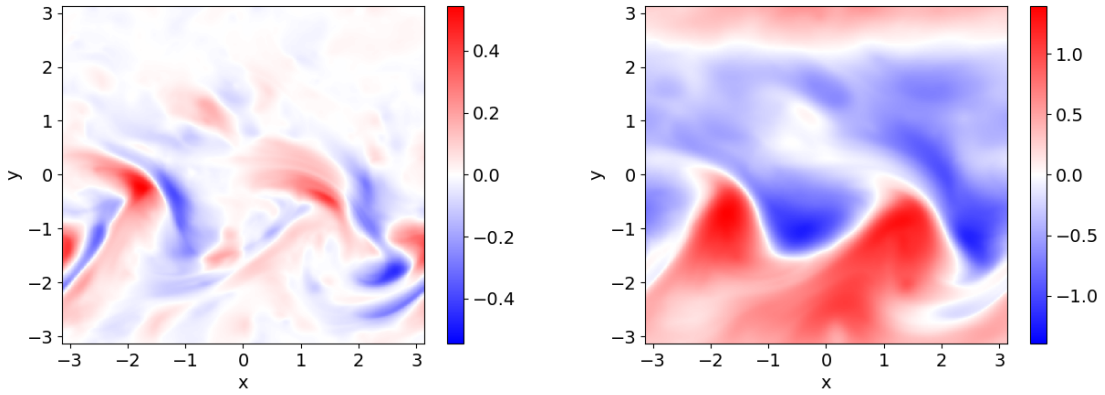

(e) q_t, $V_r = 1$ (f) M, $V_r = 1$

Figure 5: Contours of total water q_t and $M = q_t + G_M\theta_e$ for increasing V_r at time $t = 60$, after quasi-steady state has been established.

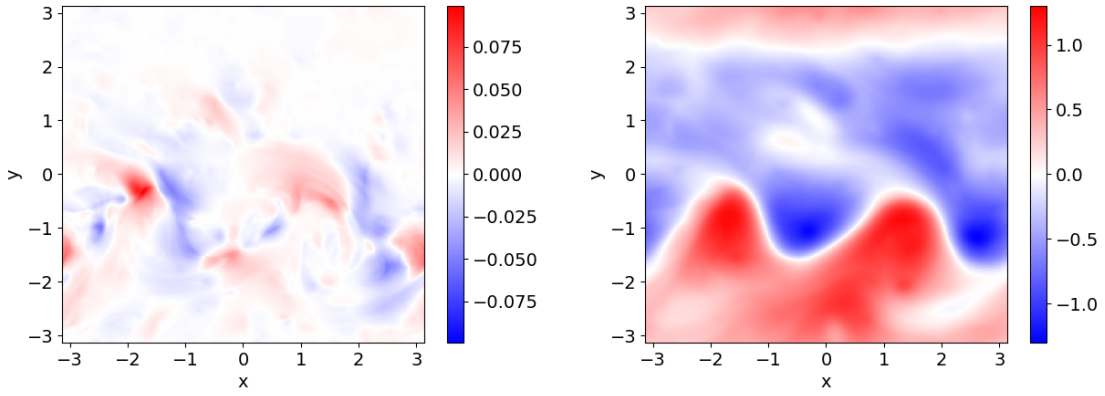

(a) q_t, $V_r = 10$

(b) M, $V_r = 10$

(c) w

(d) θ_e

Figure 6: Contours of (a) total water q_t, (b) $M = q_t + G_M\theta_e$, (c) vertical velocity w, and (d) equivalent potential temperature θ_e; the rainfall speed is fixed at $V_r = 10$. For this large V_r, the structure of q_t is similar to the structure of w; M approaches θ_e since the amplitude of $q_t \ll \theta_e$.

2.3.2 Spectra of total water

Figure 7 shows that the spectra of total water variance steepen and decrease in magnitude as rainfall speed V_r increases, reflecting the loss of fine-scale structure in q_t as well as the amplitude reduction seen in figures 5-6. To quantify the changes in the spectra, figure 8 shows the spectral exponents as a function of V_r. (The spectral exponents were computed by a linear fit from $k_h = 30 \pm 5$ to $k_h = 70 \pm 5$.) Broadly speaking, there seem to be three distinct regimes: the spectral exponent approaches the value ≈ -1.4 as $V_r \to 0$; there is a transition region for $10^{-2} < V_r < 1$; the exponent approaches the bottom dashed blue line as $V_r \to \infty$, with value close to -4. The dashed horizontal lines indicate the computed spectral exponent for w^2 (there are two lines to indicate uncertainty).

A detail that arises in figure 8 is the non-monotonic change in the spectral exponent as a function of V_r. For V_r values between roughly 10^0 to 10^1, the spectral exponent value falls below the large-V_r limiting value (about -4). To investigate whether the non-monotonicity is a numerical artifact, higher-resolution simulations were carried out with resolution of 1024^2 Fourier modes (as opposed to the standard cases with 512^2 Fourier modes), and the results are shown in figure 8 by the green marks. The higher-resolution results appear to be only slightly more monotonic, which suggests the non-monotonicity may be a natural property of the system. Further evidence is provided by comparison with the spectral exponent of θ_e and M, as shown in figure 9. Since $q_t = M - G_M\theta_e$, the spectral slope of q_t will match the shallower slope of M, which persists until around $V_r = 1$. When V_r is approximately 1, the exponent of M is approaching -5.5 or -6, which explains why the spectral exponent of q_t is able to also reach approximately -5.5.

Observational studies, for comparison, have reported spectral exponents that range as widely as -1.3 to -2.7 [Fischer et al., 2012] or -1.4 to -2.2 [Kahn and Teixeira, 2009], although the more convenient numbers of $-5/3$ and -2 are more commonly reported. Such observational ranges are more narrow than the wide range of roughly -1.4 to -4 shown in figure 8 for the model. Nevertheless, it is interesting that the model's bound of -1.4 is roughly in line with the bound that is seen in observations. Moreover, in the model a steeper spectrum can also be seen, and it is due to the influence of precipitation.

The observational spectra are influenced by numerous factors, as described in more detail in the Introduction section, and not all factors are included in the present idealized setup. In the present setup, it is mainly three parameters that could potentially influence the water spectrum: rainfall (V_r), vertical moisture gradient, and meridional moisture gradient. The latter two (the moisture gradients) will be shown in section 2.5 to have limited influence on the water spectrum. Rainfall, on the other hand, is seen to have a significant influence on the water spectrum.

To aid the comparison between observations and the present idealized model, the parameter V_r here can be viewed as an indicator of the influence of precipitation on the variability of water, in the following way. While the origin of the parameter V_r is as a representation of terminal velocity of rain, the case of $V_r = 0$ here is equivalent to the dynamics of a moist atmosphere that is always unsaturated and cloud-free. As a result, small V_r values correspond to dynamics with little or no influence of precipitation, moderate V_r values correspond with appreciable influence of precipitation, and large V_r values correspond with a dominating influence of precipitation. The correspondence between V_r in this saturated model and V_r in nature is not a perfect match, since the model here is saturated whereas nature has phase changes of water. Nevertheless, the

trends in the influence of V_r on water spectra can offer an idealized indication of trends in the influence of precipitation on water spectra.

Given this viewpoint of V_r, and given all of the factors that complicate a perfect comparison between observations and the present idealized model, it is interesting that roughly -1.4 is seen as the bound on the spectral exponent in both observations and the model, and it is seen in the model for the case of small V_r, indicating little or no influence of precipitation. Beyond this bound, steeper spectra are also seen in both observations and the present idealized model. While the steeper spectra in the model are mainly due to a larger influence of precipitation (as indicated by larger V_r values), one can expect that the steeper spectra in observations are likely influenced by precipitation as well as numerous other factors. Also, while a large range of V_r values was used here in order to explore the limiting cases, it is a smaller range of V_r values (roughly a factor of 10) that causes the large changes in the spectral exponent, ranging from -1.4 to -4 or even steeper.

From a broad point of view, the results here suggest that, even with a minimal model such as PQG, it is possible to see a wide range of exponents, broadly similar to the existence of ranges of exponents in observational data, rather than a unique, universal exponent.

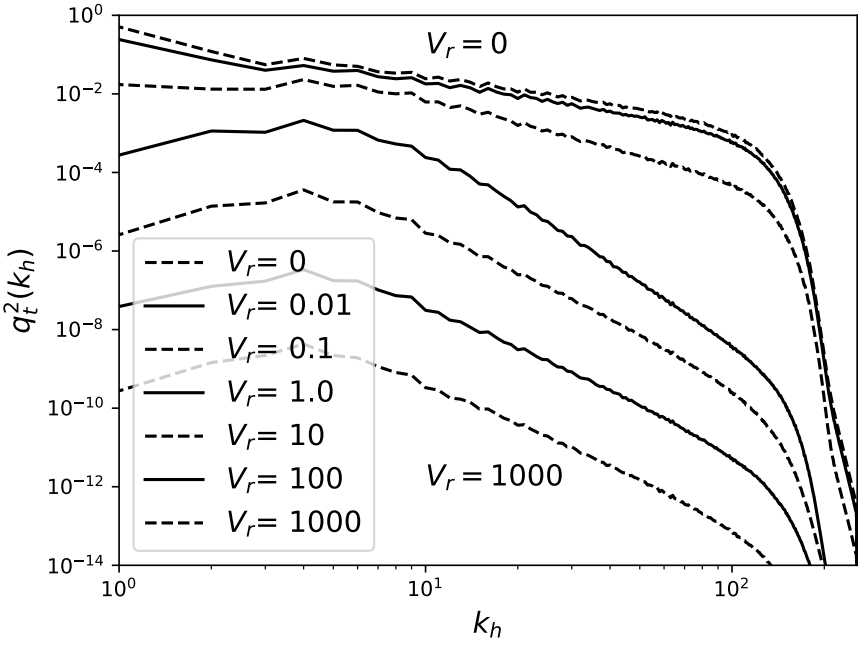

Figure 7: Spectra of total water q_t for different values of rainfall speed V_r.

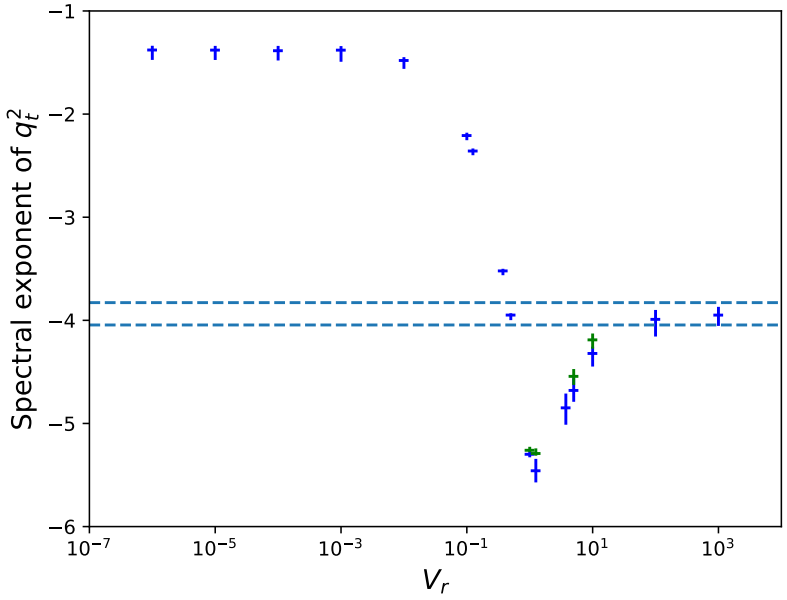

Figure 8: Spectral exponents of q_t^2 for increasing V_r, computed from figure 7 between $k_h = 30 \pm 5$ and $k_h = 70 \pm 5$. Horizontal blue line segments indicate slope values measured for $k_h \in [30, 70]$ for runs with resolution 512^2 Fourier modes; error bars are indicated by blue vertical line segments. Green line segments correspond to runs with resolution 1024^2 Fourier modes. The dashed horizontal lines indicate the computed spectral exponent for w^2 (there are two lines to indicate uncertainty).

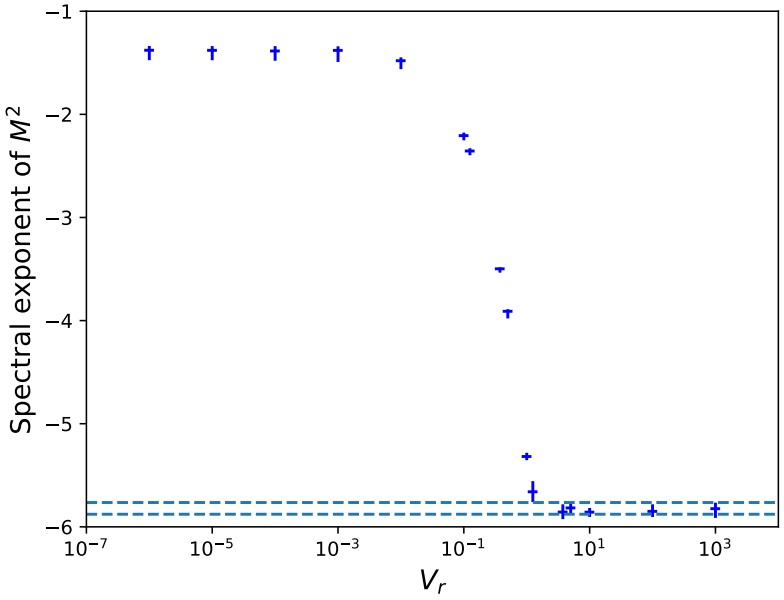

Figure 9: Spectral exponents of M^2 for increasing V_r, computed between $k_h = 30 \pm 5$ and $k_h = 70 \pm 5$. Horizontal blue line segments indicate slope values measured for $k_h \in [30, 70]$ for runs with resolution 512^2 Fourier modes; error bars are indicated by blue vertical line segments. The dashed horizontal lines indicate the computed spectral exponent for θ_e^2 (there are two lines to indicate uncertainty).

2.4 Limiting values for water spectral exponents

In this section, we use the equations of motion (2.1) and (2.6b) to help understand the limiting values of the spectral exponent for q_t^2 as $V_r \to 0$ and $V_r \to \infty$ observed in figure 8.

2.4.1 Small rainfall speed

A rudimentary understanding of the limit $V_r \to 0$ can be found from setting $V_r = 0$ in the continuously stratified PV-M equations (2.6) with $\beta = 0$. There is a well-known analogy between the PV-equation (2.6a) and the vorticity equation for 2D turbulence [Charney, 1971]. By the analogy, one may predict the scalings for the kinetic energy $KE(k_h)$ (associated with velocity) and potential energy $PE(k_h)$ (associated with θ_e) resulting from the forced-dissipative version of (2.6). The theory relies on isotropy and the existence of inertial ranges in a statistically steady state [Kraichnan, 1967]. In the inertial range of scales smaller than the forcing scales and larger than the dissipation scale, these predictions are $KE(k_h) \propto k_h^{-3}$ and $PE(k_h) \propto k_h^{-5}$, where the latter uses the relations between $\mathbf{u}, \psi, PV$ and θ_e given by (2.2) and (2.5a). The M-equation (2.6b) with $V_r = 0$ describes the evolution of a passive scalar M advected by the horizontal winds, with expected shallow spectrum $M^2(k_h) \propto k_h^{-1}$ [e.g., Babiano et al., 1987]. (The notation of $M^2(k_h), q_t^2(k_h)$ will be used to describe the power spectra of M, q_t in terms of the horizontal wavenumber.)

In the discretized 2-level equations with hyperviscosity (3.4a)-(3.4b), the Phillips

background acts as a large-scale forcing, albeit anisotropic, leading to baroclinic instability and eventually to a statistically steady state. In previous studies of both forced-dissipative 2D turbulence with $\beta \neq 0$ [e.g., Maltrud and Vallis, 1991] and 2-level QG-equations with $\beta \neq 0$ [e.g., Qi and Majda, 2016], the spectrum has been observed to be $KE \propto k_h^q$ with $-4 < q < -3$. As discussed in the latter references and many others, the anisotropy introduced by nonzero β leads to a change in flow structure from vortices to anisotropic jets, and as reproduced here in figure 3. Hence, the arguments surrounding the scalings $KE \propto k_h^{-3}$, $PE \propto k_h^{-5}$ and $M^2 \propto k_h^{-1}$ are no longer strictly valid, but the observed spectra are nevertheless not far from the predictions associated with isotropic conditions. Our simulations of (3.4) show, approximately, $KE \propto k_h^{-3.8}$, $PE \propto k_h^{-5.8}$ and $M^2 \propto k_h^{-1.4}$ (not shown). Factors contributing to steeper-than-isotropic spectra are anisotropy, structure formation and truncated vertical structure.

Finally, we can use the information about the spectral scalings for $PE(k_h)$ and $M^2(k_h)$ together with relation $q_t = M - G_M\theta_e$ to understand the spectral scaling of q_t observed in figure 8 for $V_r \to 0$. Since the potential energy spectrum $PE(k_h)$ falls off much more rapidly than the M-spectrum $M^2(k_h)$, it is clear that significantly more 'energy' is associated with M than with θ_e as soon as wavenumbers k_h are larger than the forcing scales k_f, which are the largest scales in our simulation domain. Hence, q_t inherits the fine-scale structure of M as $V_r \to 0$, and the spectrum of q_t scales as $q_t^2 \propto k_h^{-1.4}, k_h > k_f$.

2.4.2 Large rainfall speed

Consider the discretized version of equation (2.1c) for q_t at mid-height in the 2-level set-up:

$$\frac{\mathrm{D}_m q_t}{\mathrm{D}t} - G_M \frac{L_{ds}}{L} w + v Q_y = -\frac{V_r}{\Delta z} q_t. \tag{2.10}$$

We set $Q_y = 0$ for the baseline case considered above in figures 3-8. Defining $\epsilon = \frac{1}{V_r}$, the variables in 2.10 can be expanded in powers of ϵ, for example,

$$q_t = q_t^{(0)} + \epsilon q_t^{(1)} + \cdots \tag{2.11a}$$

$$\psi = \psi^{(0)} + \epsilon \psi^{(1)} + \cdots \tag{2.11b}$$

$$w = w^{(0)} + \epsilon w^{(1)} + \cdots, \tag{2.11c}$$

and so on. The order $O\left(\frac{1}{\epsilon}\right)$ balance gives

$$0 = -\frac{V_r}{\Delta z} q_t^{(0)}. \tag{2.12}$$

To leading order, then, the total water q_t is small, and its contribution at next order, $q_t^{(1)}$, satisfies the balance

$$-G_M \frac{L_{ds}}{L} w^{(0)} = -\frac{V_r}{\Delta z} q_t^{(1)}. \tag{2.13}$$

(For a more formal derivation where this limit is included as part of the distinguished limit for PQG, see Smith and Stechmann [2017].)

Accordingly, in our simulations with large V_r, we observe that the magnitude of q_t becomes small, and $q_t \sim w$, as in the time snapshot figure 6 with $V_r = 10$. Similarly, the spectral scaling exponent for the spectrum of q_t^2 approaches the exponent characterizing the spectrum w^2 as seen in figure 8.

2.5 Effects of a meridional and vertical moisture gradients

In addition to precipitation, other factors can also influence the water variance spectrum. Two such factors are the meridional moisture gradient, associated with parameter Q_y, and the vertical moisture gradient, associated with parameter G_M.

The effect of meridional moisture gradient can be studied by taking $Q_y \neq 0$ in (2.10). We explored several values of Q_y corresponding to $|Q_y| << G_M L_{ds}/L$, $|Q_y| \approx G_M L_{ds}/L$, and $|Q_y| >> G_M L_{ds}/L$.

We observed that the effects of Q_y are the most apparent for large V_r, and thus we present only this case. Returning to (2.10), the scaling $V_r = O(1/\epsilon)$ with $\epsilon \to 0$ gives $q_t^{(0)} = 0$ and the $O(1)$ balance

$$v^{(0)} Q_y - G_M \frac{L_{ds}}{L} w^{(0)} = -\frac{V_r}{\Delta z} q_t^{(1)}. \tag{2.14}$$

Now $q_t^{(1)}$ is a combination of $v^{(0)}$ and $w^{(0)}$. By changing the coefficients Q_y and $G_M L_{ds}/L$, the structure of q_t may inherit the structure of w, or the structure of v, or some combination of the two.

Single-time snapshots of w and v_m at mid-height are plotted in figure 10, so that their structure can be compared to q_t. Note that the structure of the winds does not depend on the value of V_r because of the one-way coupling. For fixed, large $V_r = 10$, figure 11 illustrates the competition between w and v for determining the structure of q_t, depending on the value of background meridional water gradient Q_y compared to $G_M L_{ds}/L$. Figure 11a is the baseline case with $Q_y = 0$, showing that q_t inherits the structure of w seen in figure 10a. However, figure 11b for $|Q_y| \approx G_M L_{ds}/L$, shows that

q_t inherits the structures of both v and w. While not as easy to see, the effects of w can be observed in figure 11b, for example in the lower right corner near $x = 1, y = -3$, there is a streak through the negative anomaly in q_t corresponding to the weak positive anomalies in w. The dual dependence of q_t on w and v can also be observed in spectra as shown in figure 12. For comparison to q_t^2, the spectra for w^2 and v^2 have been normalized by the appropriate coefficients from (2.14). For $1 \leq k_h \leq 5$, Q_y causes the q_t^2 spectra to have a similar shape to that of the v^2 spectra. However, for large k_h, the shape of the q_t^2 spectra seems to independent of Q_y. In this case of $V_r = 10$, where the rainfall speed is large, yet not so large to be near the asymptotic regime, both the q_t^2 spectra are between the normalized v^2 and w^2 spectra. If a larger value of V_r is taken, both of the q_t^2 spectra approach that of the w^2 spectra, for large k_h. One sees that the background meridional water gradient Q_y is another parameter, in addition to the parameters of the dry system and rainfall speed, V_r, which can change the characteristics of the spectral scaling for total water q_t.

Another water parameter, G_M can also effect the spectral scaling of total water. From 13, it can be seen that G_M does not have as strong an effect on the shape of the spectral curves for q_t.

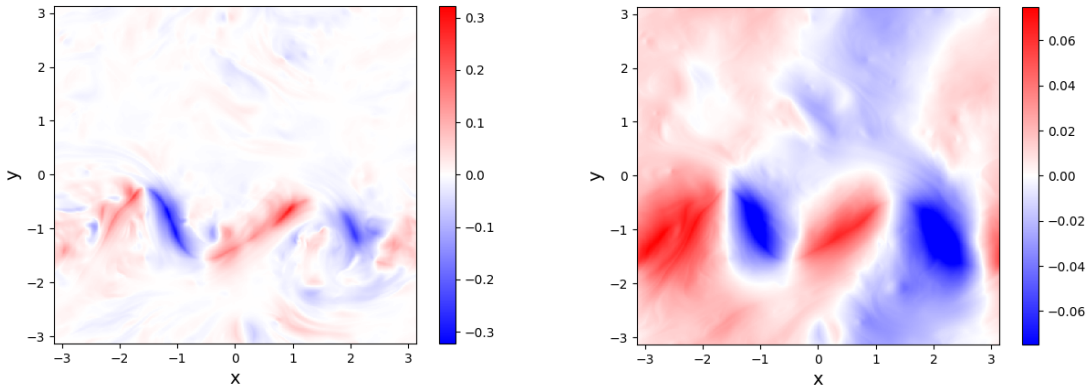

(a) $G_M \frac{L_{ds}}{L} w$ (b) $-Q_y v_m$

Figure 10: Winds at mid-height: (a) w and (b) v_m.

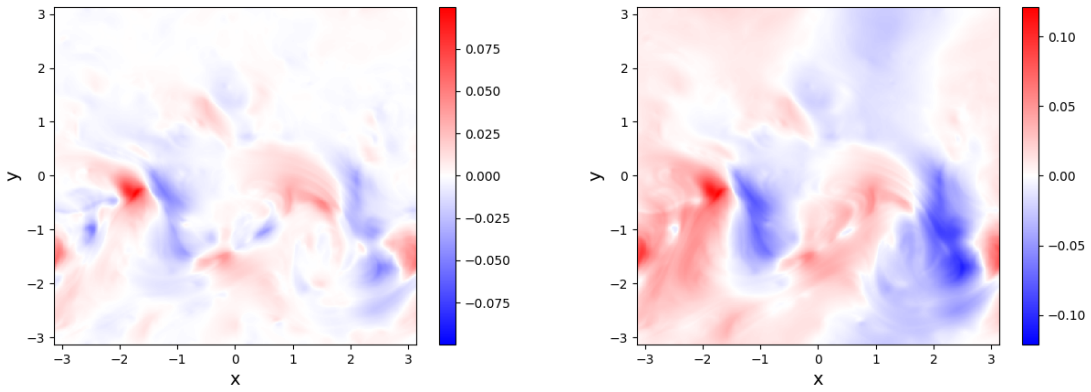

(a) q_t with $Q_y = 0$ (b) q_t with $Q_y = -1$

Figure 11: Contours of total water q_t for large $V_r = 10$: (a) $Q_y = 0$ corresponding to Phillips background with zero background meridional water gradient; (b) $|Q_y| = 1$ corresponding to Phillips background with large gradient of water in the meridional direction.

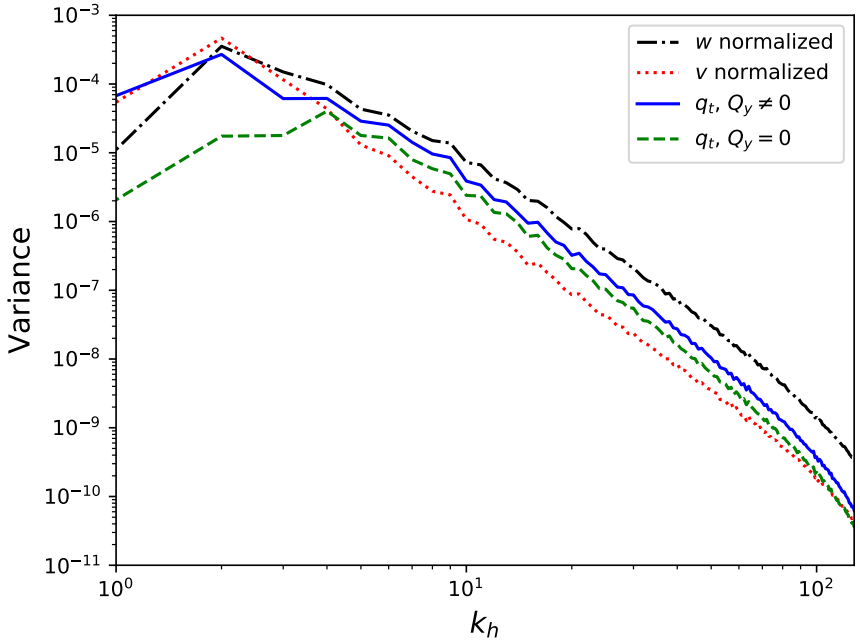

Figure 12: Velocity and total water spectra for large $V_r = 10$. Baseline case with $Q_y = 0$ (zero Phillips background water): normalized v^2 (dash-dot); q_t^2 (dot). Case $|Q_y| = 1$ (non-zero meridional gradient of Phillips background water): normalized w^2 (solid); q_t^2 (dashed). For even larger values of V_r, the slope at large wavenumbers for both q_t spectra approach that of w.

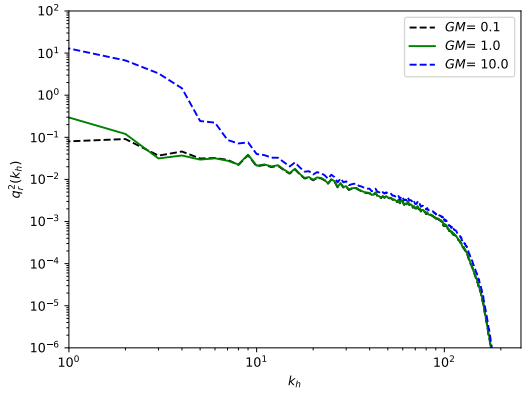

(a) $V_r = 0.001$

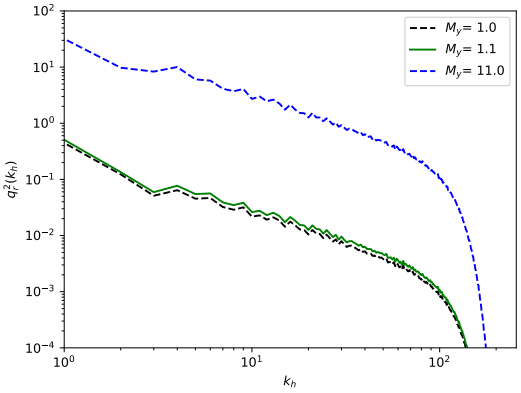

(b) $V_r = 0.001$

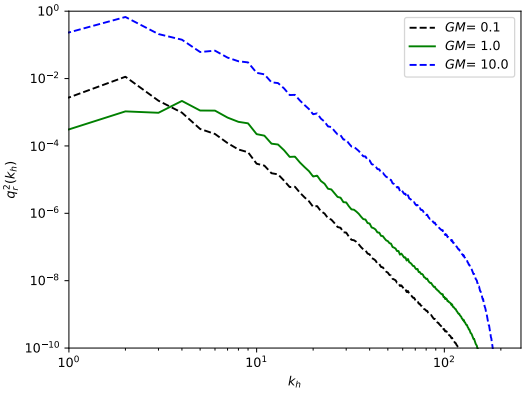

(c) $V_r = 1$

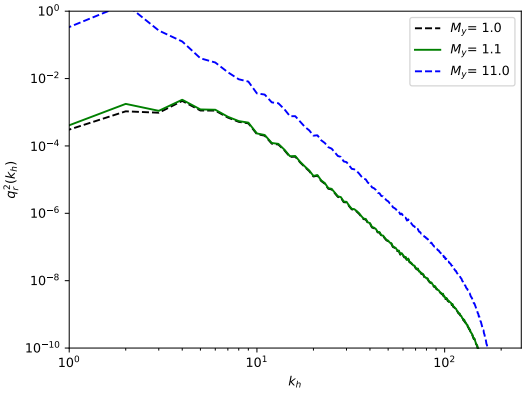

(d) $V_r = 1$

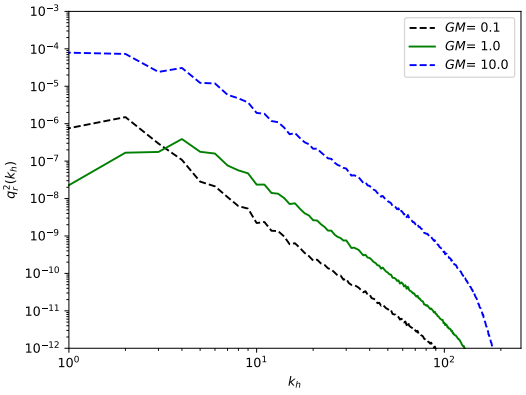

(e) $V_r = 100$

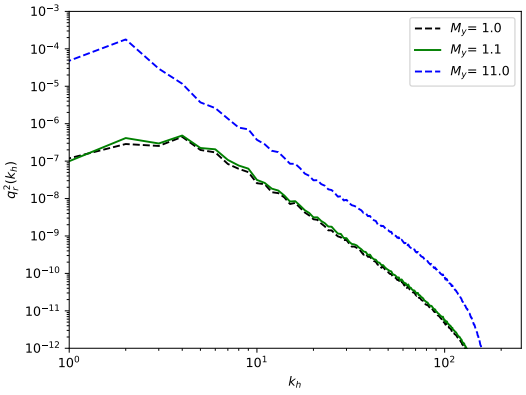

(f) $V_r = 100$

Figure 13: Left column represents the change of the spectra based on changes in G_M and the right column represents that by changes in M_y. (Larger values of G_M, M_y correspond to curves higher up. The parameters G_M, M_y do not effect the behavior of the q_t spectra at high wave numbers. For low wave-numbers, we do see some difference, which can be explained from the combination of θ_e, M. (Note $M_y = (\cdot)$ should be considered as $M_y = (\cdot)\times$base value. $M_y = 1.1$ corresponds with $Q_y = 0.1$.)

2.6 Discussion and Conclusion

In summary, we have investigated the organization and structure of water in simulations of geostrophic turbulence. As there is no definitive variance spectrum from observational data of water, we also explored possible influences on the ranges in variance spectrum observed. This was done by using the PQG model which is based on a quasigeostrophic approach. While this PQG model has the usual limitations from QG along with those from having coarse vertical resolution due to being two-leveled, it provides a simple framework for understanding one aspect of how water behaves.

A main focus was to study the influence of precipitation on the variability of water. In the simple model setup here, the influence of precipitation can be controlled by varying the rainfall speed parameter, V_r, and it was seen that different behaviors can observed: small V_r leads to a prominent small-scale structure of water, while larger V_r essentially filters out the small scales. The model showed that for small V_r, a spectral exponent for q_t will be between -2 and -1, and for large V_r, the spectrum slope will approach that of w. Moreover, theoretical arguments provided explanations for these two asymptotic limits.

While it is natural to search for a clean fractional value for the spectral exponent, the results here are in line with the view that the spectral exponent in nature may not have a simple fractional value, as even with a PQG model which contains few parameters, by just adjusting the value of one, V_r, a continuum of possible spectral exponent values is obtained, ranging from around -1.4 to around -5. Moreover, with a presence of a meridional gradient of water, one can adjust the balance between the vertical and meridional to obtain a q_t which appears to be a combination of v and w in

the limit of large V_r. In the case of comparable water gradients, there is a possibility that q_t will appear like v for a certain range and w for another, although this would require further investigation to understand in more detail.

Wave or mode decompositions provided a key perspective here for understanding water. In particular, it was shown that the water q_t could be written as a linear combination of two other variables: a passive tracer M and an active tracer θ_e, which correspond to a moist eigenmode and the vortical mode, respectively. In the case where the passive tracer is different from the active tracer, i.e. the small V_r regime, we saw that in our case, q_t behaved more as a passive tracer. In the case where the passive tracer was forced to relax towards the active tracer, q_t behaved as the difference between the passive tracer and active tracer, which in our case was w.

With the ability to provide a continuum of behavior for water while also providing asymptotic limits to the behavior, this study suggests that the two level PQG model provides a useful framework to study water in the atmosphere. In the future, it would be interesting to use the full version of the PQG equations including phase changes [Smith and Stechmann, 2017], which would offer additional realism to the model, but likely at the expense of complicating theoretical analyses.

Chapter 3

Atmospheric Water transport

3.1 Introduction

Moisture transport in the atmosphere is important as it connects the evaporation of water in the oceans to precipitation over land. With more understanding of the physical processes involved in moisture transport, there could be improved forecasts of precipitation. Two important large-scale dynamical structures for moisture transport are the low-level jets (LLJ), in the tropics and subtropics, and the Atmospheric Rivers (AR) mostly in the extra-tropics [Gimeno et al., 2016]. In this present paper, we will focus on meridional moisture transport in the mid-latitudes using a quasi-geostrophic framework. As such, we will be investigating ARs in a QG setting and some more general properties of meridional moisture transport.

Atmospheric Rivers (ARs) are an important source of water transport in the atmosphere. They can carry more water than 7-15 Mississippi Rivers combined [Ralph and Dettinger, 2011] and are reported to be able to transport more than 90% of the total mid-latitude vertically integrated water vapor flux [Zhu and Newell, Gimeno et al., 2014]. Due to the amount of water within these ARs, when one passes by a coastal area, it can provide significant amounts of precipitation. For example, a study by Smith et al. [2010] saw that about 20-40% of the water vapor in an atmospheric river rained

out over northern California. Moreover, in these locations, a significant portion of the annual precipitation is due to AR contributions [Dettinger, 2011, Ralph et al., 2013, Rutz et al., 2014].

ARs are defined in the Glossary of Meterology to be "a long, narrow, and transient corridor of strong horizontal water vapor transport that is typically associated with a low-level jet stream ahead of the cold front of an extratrpoical cyclone" [Ralph et al., 2018]. The studies of ARs are mostly done on observational data or on data from complex models. In this present paper, the overarching questions are: Can atmospheric rivers form in a simple model, and if so how much of a contributing factor are they to meridional moisture transport in a simple model? To investigate this question, a quasi-geostrophic (QG) framework is used as it is simple enough to understand theoretically, yet complex enough to have interesting behavior. Some examples of past achievements of the quasi-geostrophic equations are the explaining baroclinic instability [Charney, 1947, 1948, Phillips, 1954] and geostrophic turbulence [Rhines, 1979, Salmon, 1980]. As such, it is reasonable to hope that further understanding of ARs and water flux can be achieved in a similar framework.

As a quasi-geostrophic model with water, the recently derived precipitating quasi-geostrophic (PQG) equations will be used [Smith and Stechmann, 2017]. For comparison, there have been other variations/adaptations of the dry QG equations to include moisture and moisture effects via latent heat release, etc. [e.g., Mak, 1982, Bannon, 1986, Lapeyre and Held, 2004, Monteiro and Sukhatme, 2016]; these and other similar models [e.g., Lambaerts et al., 2012] have provided insight into moisture dynamics and the role of latent heat release in the atmosphere. One distinguishing and advantageous property of the PQG equations is that they are asymptotic limiting equations. Specifically,

the PQG equations arise in the limit of rapid rotation and strong (moist) stratification, starting from the equations for midlatitude dynamics with moisture, phase changes, and precipitation [Hernandez-Duenas et al., 2013]. In Wetzel et al. [2017], moisture transport in PQG was examined for the linearized equations in a single phase.

In this paper, we show that even with a simple model with only one phase, the presence of ARs, as well as the fact that some of these ARs can represent a large percentage of the meridional flux. We also show the effects of some of the parameters on the meridional water fluxes. In particular, the effects of two parameters, the meridional gradient of water and the rainfall speed are shown to have a non-negligible impact on water transport.

The paper is organized as follows. In section 2, the precipitating quasi-geostrophic equations (PQG) are introduced. Section 3 describes the numerical method used to solve the PQG system, and also the algorithm used to identify the QG atmospheric rivers. In section 4, there is a discussion on the characteristics of the atmospheric rivers. In section 5 properties of the meridional transport of water as well as the effects rainfall and meridional moisutre gradient on the meridional moisture transport is examined , and the discussion and conclusion is in section 6.

3.2 Description of Precipitating QG Equations

The PQG equations can be considered as a moist version of the QG equations. The QG equations describe the slow evolution of synoptic-scale flows under assumptions of rapid rotation and strong stratification. Derivations for the dry QG equations can be found in Salmon [1998], Vallis [2006], Pedlosky [2013].

The starting point for the derivation of the precipitating quasigeostrophic (PQG) equations is a simplified cloud resolving model. Conversions between water vapor, cloud water and rain water are modeled at macroscopic scales and for each conversion process, a time scale is associated with it. In a quasigeostrophic framework, these processes are taken to be instantaneous as these time scales are much smaller compared to the time scales associated with rotation, buoyancy effects, advection, and rain fall in the mid-latitude. These assumptions of fast cloud microphysics leads to the FARE model (fast auto-conversion and rain evaporation) [Hernandez-Duenas et al., 2013] which can be considered as a moist version of the Boussinesq equations used to obtain the PQG equations.

Beyond the assumptions of the dry QG framework (rapid rotation and strong dry stratification), an additional assumption in the PQG framework is a strong moist stratification of equivalent potential temperature [Smith and Stechmann, 2017, Wetzel et al., 2017]. In PQG, boundaries between unsaturated and saturated flow regions are represented by Heaviside nonlinear switches: water below the saturation level exists in the vapor phase only; water above the saturation level is instantaneously converted to rain water, which falls at a constant speed V_r. More detailed derivations of the PQG equation and the vertically finite differenced version can be found respectively in Smith and Stechmann [2017] and chapter 2.

Now as we are considering only the case with no phase changes the anomolous total water, q_t is equivalent to anomolous rain water, q_r

$$q_t = q_r \tag{3.1}$$

so from here on all q_r values will be replaced with q_t.

Similar to the dry case, by taking a finite difference in z with two levels, the two level PQG equations can be obtained,

$$\frac{\mathrm{D}_1 PV_1}{\mathrm{D}t} + \beta v_1 = 0 \tag{3.2a}$$

$$\frac{\mathrm{D}_2 PV_2}{\mathrm{D}t} + \beta v_2 = 0 \tag{3.2b}$$

$$\frac{\mathrm{D}_m M_m}{\mathrm{D}t} = -\frac{V_r}{\Delta z} q_{r,m} = -\frac{V_r}{\Delta z}(M_m - G_M \theta_{e,m}) \tag{3.2c}$$

with

$$PV_1 = \nabla_h^2 \psi_1 + \left(\frac{1}{\Delta z}\frac{L}{L_{ds}}\right)^2 (\psi_2 - \psi_1) \tag{3.3a}$$

$$PV_2 = \nabla_h^2 \psi_2 + \left(\frac{1}{\Delta z}\frac{L}{L_{ds}}\right)^2 (\psi_1 - \psi_2) \tag{3.3b}$$

$$\theta_{e,m} = \frac{L}{L_{ds}}\frac{\psi_2 - \psi_1}{\Delta z} \tag{3.3c}$$

$$u_i = -\frac{\partial \psi_i}{\partial y} \text{ for } i = 1, 2 \tag{3.3d}$$

$$v_i = \frac{\partial \psi_i}{\partial x} \text{ for } i = 1, 2 \tag{3.3e}$$

$$u_m = \frac{u_1 + u_2}{2} \tag{3.3f}$$

$$v_m = \frac{v_1 + v_2}{2}. \tag{3.3g}$$

where u_i, v_i, ψ_j, for $j = 1, 2$ and $\theta_{e,m}, M_m, q_t, q_r$ are functions of two spatial variables (x, y) and time, t; u_i, v_i represent the horizontal components of the fluid velocity at level j; $\theta_{e,m}$ represents the equivalent potential temperature at the mid-level; $q_{t,m}$, $q_{r,m}$ represent the total water and rain water at the mid-level respectively. In the QG, the (depth) averaged velocities u_m and v_m are commonly known as the barotropic velocities. Summaries of the variables, parameters, and symbols are provided in Tables 1–4. From

here on, the subscript m will be omitted from the thermodynamic variables θ_e, M, q_t to reduce notation.

We use the notation $\frac{\mathrm{D}_1}{\mathrm{D}t}(\cdot) = \partial_t(\cdot) + u_1\partial_x(\cdot) + v_1\partial_y(\cdot)$, and similarly for $\frac{\mathrm{D}_2}{\mathrm{D}t}(\cdot)$ and $\frac{\mathrm{D}_m}{\mathrm{D}t}(\cdot)$.

During the finite differencing, vertical boundary conditions of a rigid lid, $w = 0$ is imposed on the top and bottom boundaries, and as well as a condition of no inflow of q_t from the top. Periodic boundary conditions are imposed in the horizontal direction.

In these equations, there are four nondimensional parameters in the PQG equations: the length-scale ratio L_{ds}/L; change in the rotation rate with latitude, β; the rainfall speed, V_r; and the scaled ratio of the background vertical gradients of total water and equivalent potential temperature, G_M. In section 3, a fifth nondimensional parameter, the meridional gradient of water, Q_y is included.

3.3 Methods and Numerics

3.3.1 Numerics for simulation

Our main goal is to investigate the structure and statistics of ARs as water transport in a statistically quasi-steady state of saturated PQG, evolving from baroclinically unstable initial conditions. To do so, we numerically computed the solution to equation 3.2 with additional dissipation terms given by 4th-order hyperviscosity and lower-level friction. The model used is the same as that used in chapter 2:

$$\frac{\mathrm{D}_1 PV_1}{\mathrm{D}t} - U\partial_x PV_1 + v_1\partial_y PV_{1,bg} + \beta v_1 = -\kappa_M \Delta\psi_1 - \nu\Delta^4 PV_1 \tag{3.4a}$$

$$\frac{\mathrm{D}_2 PV_2}{\mathrm{D}t} + U\partial_x PV_2 + v_2 \partial_y PV_{2,bg} + \beta v_2 = -\nu\Delta^4 PV_2 \tag{3.4b}$$

$$\frac{\mathrm{D}_m M}{\mathrm{D}t} + v_m \partial_y M_{bg} = -\frac{V_r}{\Delta z}\left(M - G_M \theta_e\right) - \nu\Delta^4 M. \tag{3.4c}$$

The parameter values $\beta = 2.5$, $\kappa_M = 0.05$, $\nu = 5 \times 10^{-15}$ and $k_{ds} = 4$ were chosen to match the (dry) mid-latitude atmosphere case studied in Qi and Majda [2016]. Instead of the value $U = 0.2$ as in their study, the parameter value $U = 0.25$, was chosen as it produced a jet which had more movement which appeared to better allow atmospheric rivers to form in our simulations. The parameters reflecting the presence of water in our 2-level PQG equations are G_M and V_r: G_M depends on the background water profile and V_r is the rainfall speed. In the present study, we fix the value $G_M = 1$ and vary V_r. The baseline case has background meridional gradient $Q_y = -1$ such that $M_{bg} = (Q_y + G_M\Theta)y = -1 + G_M\Theta y$.

A pseudospectral solver was used to solve (3.4) on a doubly periodic, horizontal domain. The time-stepping was done according to a 3rd-order Runge-Kutta scheme with an adaptive Δt chosen to satisfy the CFL condition. Three-halfs padding was used for de-aliasing. Most of the simulations used resolution $N^2 = 256^2$ Fourier modes, with a few higher-resolution simulations as described below for about 400 days. The initial condition was a band of eigenmodes centered around the unstable wave-vector $(k, l) = (3, 1)$, and the simulations were run long enough to obtain statistical steady states. These eigenmodes can be obtained by solving the linearized equation (see chapter 2 for more details on the linearized equations). In addition to the two modes obtained from the PV equations, as done in dry QG, there is another eigenmode from the M equation that is not present in dry QG.

3.3.2 Atmospheric River Identification Algorithm

There are several methods to identify ARs, most of which depend on intensity and/or geometry thresholds. These can be largely split into three categories [Guan and Waliser, 2015]: (1) methods which use a single observation site or model grid cell, [e.g. in Neiman et al., 2009, Dettinger, 2011, Ralph et al., 2013] (2) methods which track pre-selected cross-sections while satisfying a set criteria for the geometry and intensity, [e.g. in Lavers et al., 2011, 2012, Nayak et al., 2014, Gao et al., 2015] (3) methods which consider geometry and intensity thresholds throughout the domain and identifying any ARs in the domain [e.g. in Wick et al., 2013, Jiang et al., 2014, Rutz et al., 2014, Guan and Waliser, 2015]. The first method is useful for studying AR landfalls in small, local areas; the second method is useful for regional studies concerning AR landfalls; and the third method for larger domains, where the interest is not only on AR landfalls.

In addition, there is also a choice in variable between using integrated water vapor (IWV) and integrated vapor transport (IVT). Initially, IWV was used to identify and measure the AR's intensity and spatial distribution [e.g. in Ralph et al., 2004, Neiman et al., 2008] since these studies used satellite-based observations. However, more recently, IVT is used as it is more directly related to precipitation outcomes and as it depends less on surface elevation [e.g. in Rutz et al., 2014, Ralph et al., 2019].

In this manuscript, the identifying atmospheric rivers is essentially based on the algorithm mentioned in Guan and Waliser [2015], which is a method in the third family which can be used to study large scales, and does not require a pre-selection of a cross-section. To be consistent with their algorithm, we also chose IVT to be the variable of interest over IWT. As our model only has $q_t(z)$ at $z = z_m$ (at the midlevel), the q_t will

be assumed to be independent of z for simplicity.

The general idea of the algorithm is to identify locations with high intensity of IVT with specific geometries (long and thin) where the direction of the IVT corresponds with the direction of the geometry. Further details are in the next paragraph. A key difference from Guan and Waliser [2015] is that they use a length criterion of having at least 2000km, whereas in our case, we use adjusted the criterion to 1000km as the domain is smaller.

The algorithm is as follows.

First to find high intensity IVT regions, connected regions in which the magnitude of the water transport is at least at the 85th percentile are identified. The mean water transport direction is then determined for each of these regions and compared to the water transport direction in each cell. If more than half of the grid cells deviate by more than 45^o from the mean water transport direction, this region is removed from the possible candidates for an AR.

To determine if the high intensity IVT regions have the correct geometry, the line which connects the two points which are furthest apart from each other, known as the major axis, is first identified. If the orientation of the major axis differs from the direction of the mean water transport direction by more than 45^o, this region is also discarded. The length is considered to be the length of the major axis for each region. The width is computed by taking the area of each candidate region and dividing by the length. If the candidate region has a length greater than the length threshold, and if it also has a ratio of length/width greater than 2, than we define this to be an AR. As mentioned above, in Guan and Waliser [2015] a length threshold of having at least 2000km is used, whereas in our case, as the domain is smaller, we use adjusted the criterion to 1000km.

3.4 Characteristics of QG atmospheric rivers

In this section we explore to what extent do atmospheric rivers appear in this model, and the characteristics that these ARs have compared to nature. Furthermore, we explore the effect of varying the rainfall parameter, V_r on the occurrences of the rivers.

In nature, most ARs appear as very long and thin corridors of water transport, a typical example being a long filament reaching from the Hawaiian islands to northern California. Moreover, ARs are known to carry a large percentage of meridional flux [Zhu and Newell], which will be explored in the next section. There is a tendency for ARs to appear more frequently in the winter, due to the strong association with extra-tropical cyclones [Gimeno et al., 2014]. For the time period between 2008-2010, Waliser et al. [2012] counted a total of 259 ARs (for the first year, 122; for the second, 137), in roughly 5 different regions (North-East Pacific, South-East Pacific, North Atlantic, South Atlantic, South Indian) of which approximately a quarter make landfall. It has been suggested in Bao et al. [2006], Dacre et al. [2015] that ARs could also form and be maintained due to individual cyclones which accumulates moisture ahead of the cold front at the base of a warm conveyor belt airflow.

We present two examples of ARs which were identified by the algorithm mentioned in section 3.2. Figures 14 and 15 show the anomalous total water, q_t and the zonal velocity, u_m which advects the q_t in two different times and instances of the simulations. Both figures show areas where there are filamentary regions of q_t which roughly correspond to the edges of the eastward zonal jet. Away from the zonal jet, the q_t anomalies are weaker and less filamented.

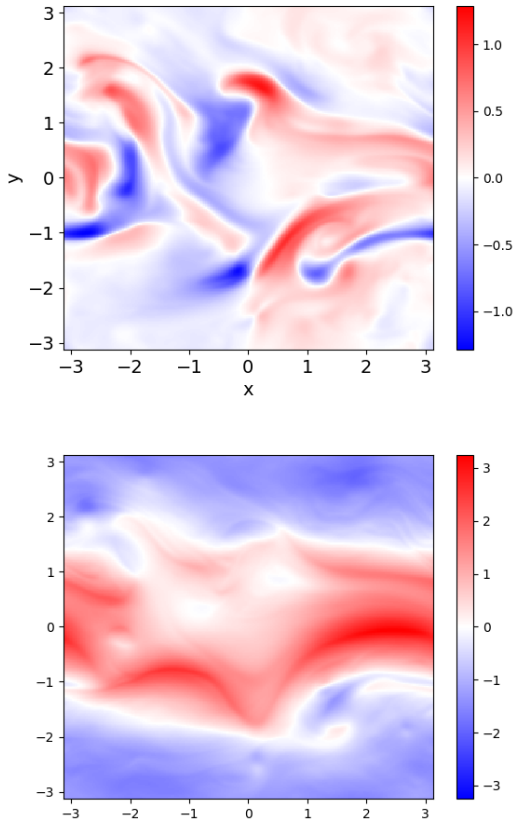

Figure 14: Example 1: Snapshot of q_t (top) and u_m (bottom) $t = 360$

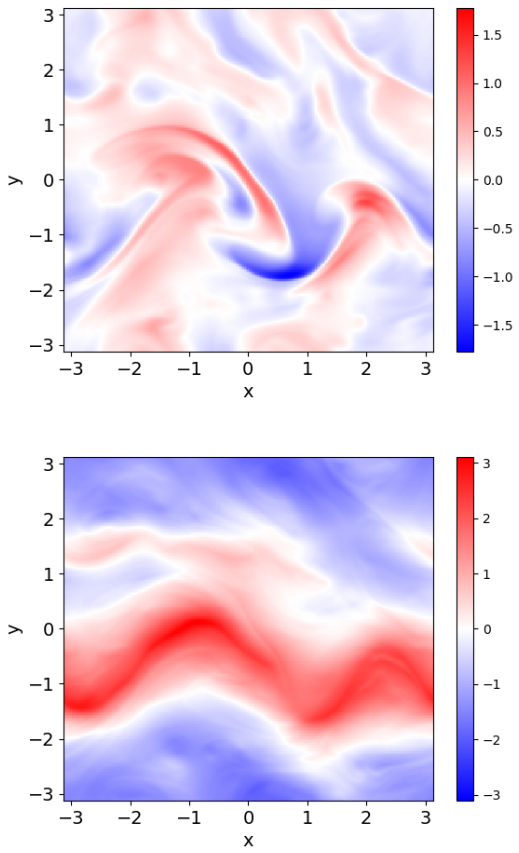

Figure 15: Example 2: Snapshot of q_t (top) and u_m (bottom)

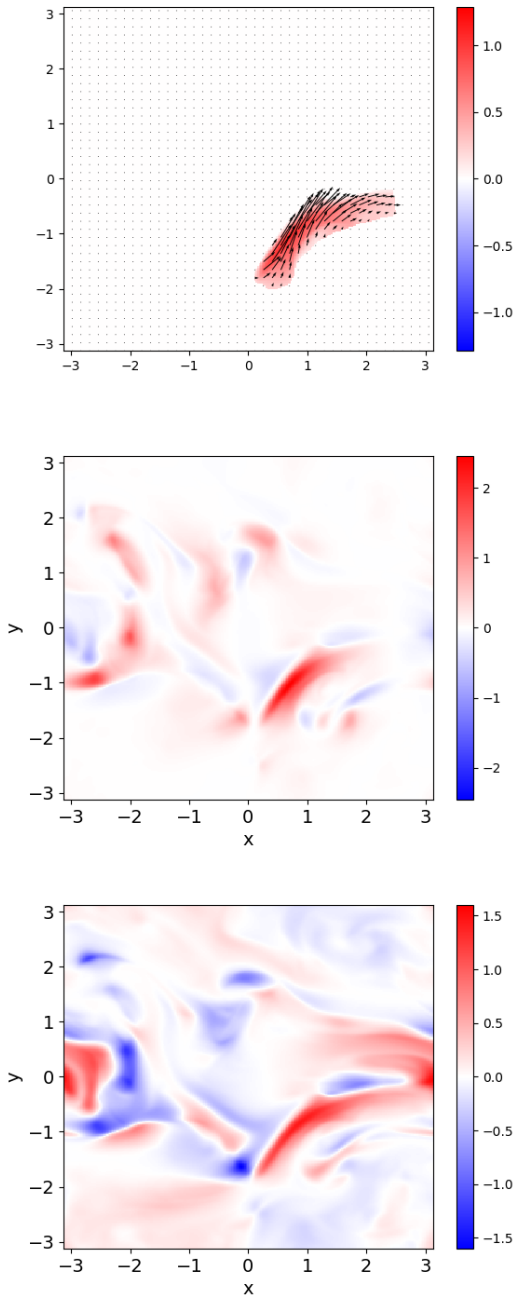

Figure 16: Example 1: Snapshot of river (top), vq_t (middle), uq_t (bottom) $t = 360$

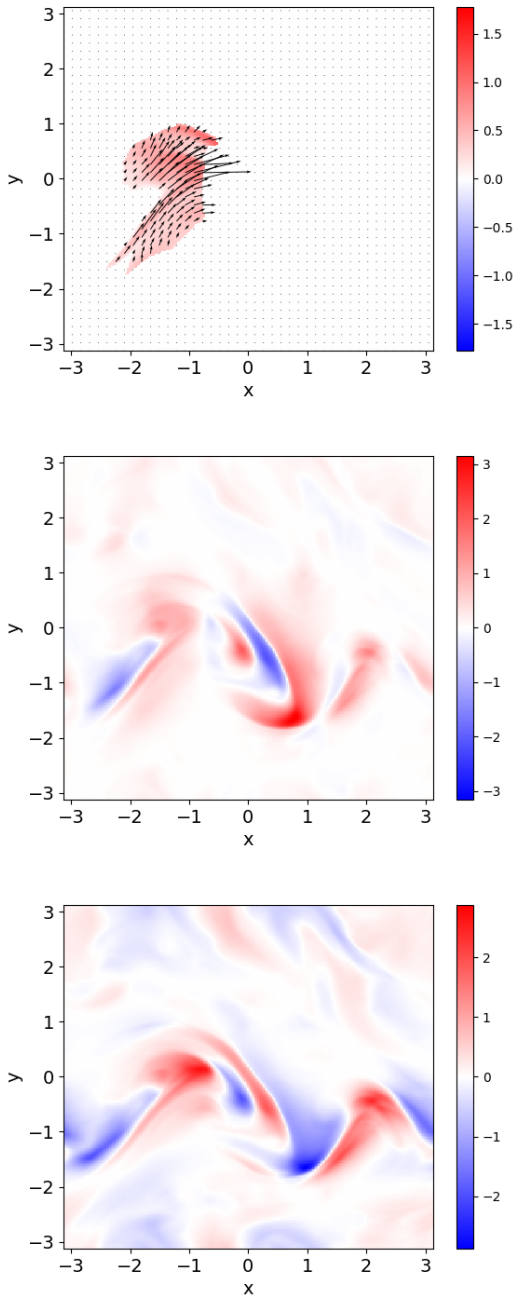

Figure 17: Example 2: Snapshot of river (top), vq_t (middle), uq_t (bottom) $t = 700$

Figures 16 and 17 show the ARs which were identified and the accompanying snapshots of uq_t and vq_t. The regions of strongest water transport in the x and y direction are, as one would expect, regions where q_t and u, v are strong, which in these cases appear to correspond with the location of the zonal jet. The AR in figure 16 especially shows that these structures can appear to be long and filamented, like those which can be seen in nature. Several factors can cause regions of strong filamented q_t to not be identified as ARs due to the criteria and algorithm that we are using. Some reasons are: the direction of water transport does not roughly align with the geometry of the region; the region could have weak winds resulting in weak water transport; the region is too small to be considered, etc. In this case, the uq_t, vq_t snapshots would be better indicators for regions which could potentially be identified as ARs.

It is important to note, however, that the model lacks phase changes and fronts, so one cannot expect all the ARs in these simulations to have the exact same properties as the ARs seen in nature.

In figure 18, the effect of the rainfall parameter, V_r, on the number of ARs seen is presented below. To ensure that there we do not count the same ARs twice, we run the algorithm on snapshots which are taken 20 time units apart (one time unit corresponds to around one day). For each V_r value, 10 simulations are run and the minimum and maximum number of ARs are shown by the vertical line. The circle represents the average number of ARs observed.

From this figure, it is observed that for V_r values which are not too large, the number of atmospheric rivers are within the range of observational values of ARs seen in one region, which observe around 5 to 20 atmospheric rivers per year [Byna et al., 2011, Lavers et al., 2012]. This is due to large V_r causing q_t to have similar structure to w as

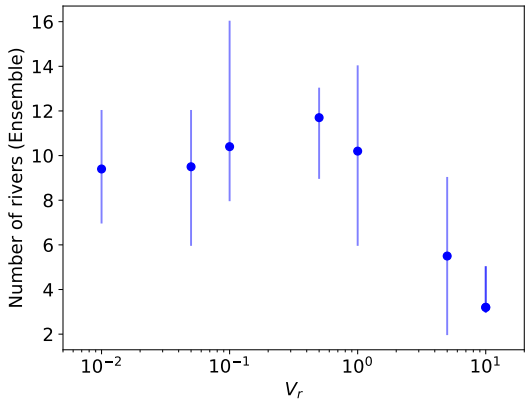

Figure 18: Number of atmospheric rivers observed as a function of the rainfall speed parameter, V_r. $Q_y = 1$. The horizontal bar indicates the average number of rivers from the simulations.

mentioned in chapter 2. Moreover, from the same chapter it is known the if V_r is very small, q_t will appear to only have filamented structure and lack some of the larger scale structure, and so would not be a good candidate to use the AR identification algorithm.

In the next section, we will consider what percentage of the meridional flux are in the ARs which are identified.

3.5 Meridional water transport

In this section, we explore the characteristics of the meridional water transport, the impact of the moist parameters of the meridional gradient of water and the rainfall parameter on the meridional water transport, and also, the amount of meridional transport seen in an AR compared to the total meridional water transport in this model.

It has been reported that atmospheric rivers can provide more than 90% of the total mid-latitude vertically integrated water vapor flux Zhu and Newell, Gimeno et al. [2014]. Splitting the total water flux Q_t, into a "broad flux," Q_b and a "river flux", Q_r as done in Zhu and Newell, we also observe that Q_r can be a large portion of the zonally averaged meridional flux. This splitting is computed by

$$Q_r \geq Q_{mean} + 0.3(Q_{max} - Q_{mean}) \tag{3.5}$$

where Q_r is the water flux at a given point, Q_{mean} is the zonally averaged magnitude of the water flux and Q_{max} is the maximum zonally averaged magnitude of the water flux for a given latitude. If the inequality holds, the point is considered to be part of the river flux.

Figure 19 shows the the result of using this splitting on example 1. The river identified by the algorithm from 3.2 is shown in the "river flux" plot. As can be seen from figure 20 the "river flux" can contain much of the meridional flux, as was observed in Zhu and Newell. For example, near the latitude $y = -1$ which corresponds with the location of the AR from example 1, the meridional river flux is around 66% of the total meridional flux. Note that the regions near the edges of the zonal jet ($y = -1.5$ and $y = 1.5$) contain the strongest zonally-averaged meridional flux.

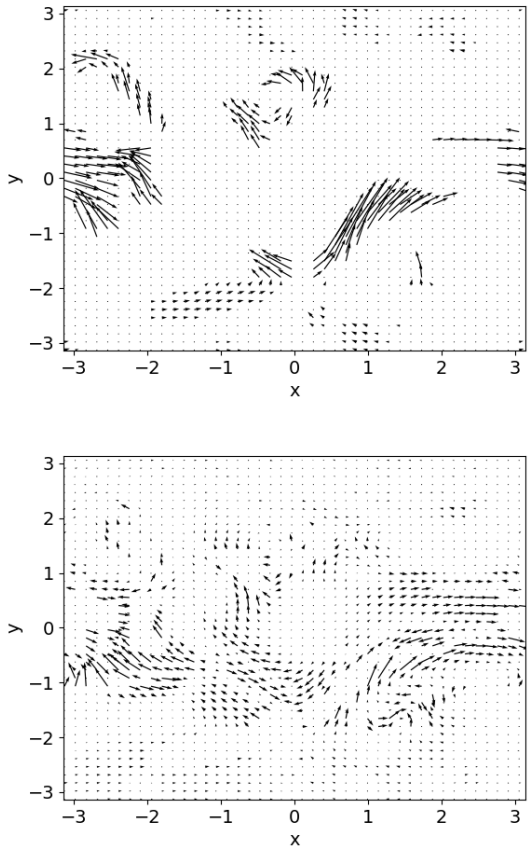

Figure 19: The "river flux" (top) and "broad flux" (bottom) determined from Zhu and Newell

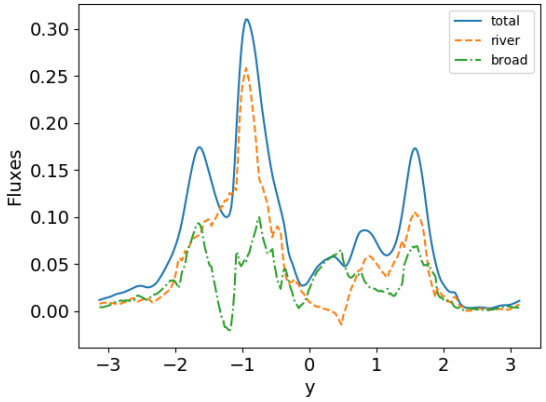

Figure 20: Zonally averaged meridional fluxes where "rivers" are identified by a cutoff mentioned in Zhu and Newell

To more precisely determine the amount of meridional water flux which is due to the ARs, the ratio between the total meridional water flux in the ARs by the algorithm in 3.2 can be compared to the total meridional water flux of the whole domain. The ratio of the meridional flux from the atmospheric river is calculated by

$$P = < vq_r >_{river} / < vq_r >_{total} . \tag{3.6}$$

For the case of $V_r = 1$, values of P ranged from 0.06 to 0.46, with most of the values around 0.20-0.30. For $V_r = 0.1$ values of P ranged from 0.05 - 1.26, with most values near 0.30-0.50. Values greater than 1.00 indicate that there were a higher amount meridional water flux in the river than the total meridional water flux in some instances. Although the ARs only take up a fraction of the space as seen from figures 16 and 17, we see that even in a simple model they can contribute a disproportionate amount of the meridional transport of water.

The behavior of the meridional water flux over time is illustrated below. Figure 21 shows the total meridional θ_e flux, $< v\theta_e >$ and total meridional water flux, $< vq_t >$ as a function of time, for a long time simulation for the standard case, with $V_r = 1$. The two lines in each plot indicate the total flux and the positive flux (e.g. $< vq_t >_{total} = < vq_t >_{positive} - | < vq_t >_{negative} |$). This is meant to show how much of the total flux can be attributed to the positive flux. The smaller distance between the total and positive flux indicates that there is less negative flux; and in contrast, the further apart the total and positive flux, the more negative flux there is. An interesting feature of this figure is that the spikes in the total meridional water flux corresponds to the spikes in the total meridional θ_e flux.

For a better understanding of the behavior of some of the dry and moist variables,

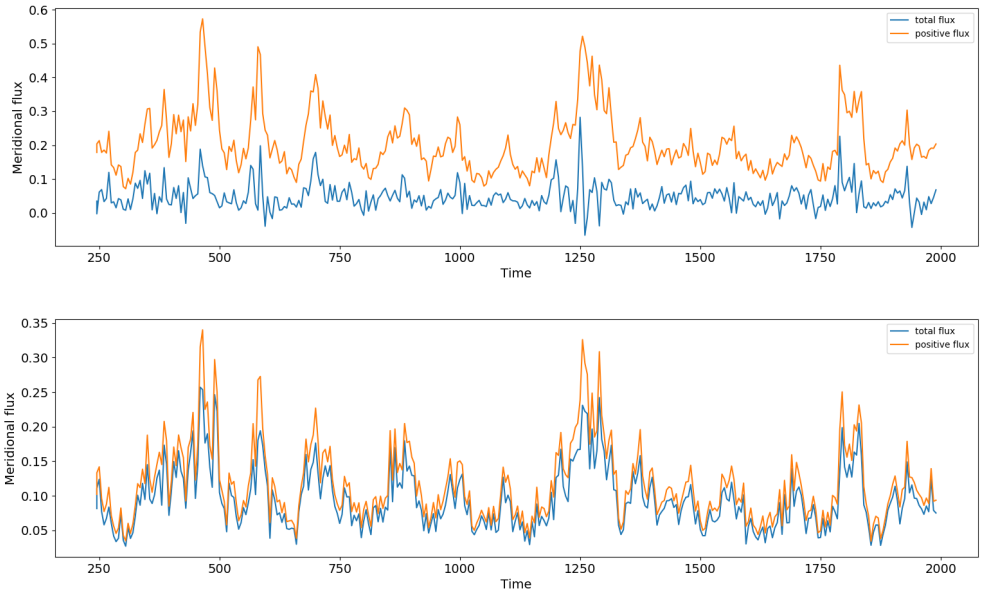

Figure 21: The total meridional θ_e flux $< v\theta_e >$ (top) and total meridional water flux $< vq_t >$ as a function of time.(long time)

the zonal averages of u_m, θ_e, q_t, vq_t are presented in Figure 22. The location of the spikes in the meridional fluxes in figure 21 seem to correspond with the change in behavior of the flow, where the zonal jet starts to change direction. The zonal jet can be seen in the top plot, which shows zonally averaged u_m. The zonally averaged potential temperature appears to also have the jet-like structure, with a phase-shift in the $y-$direction. Moreover, we observe in the third plot that there is strong positive q_t above the eastward jet and negative q_t below the jet, and in the fourth plot, that the meridional transport of water is strongest where the eastward jet is located.

Referring back to figure 21, we observe that for $< vq_r >$ total meridional flux is always positive, and that there is very little negative flux as can be seen by the two lines almost overlapping with each other. By changing the values of the two moist parameters the meridional moisture gradient, Q_y, and the rainfall parameter, V_r, the effects on the

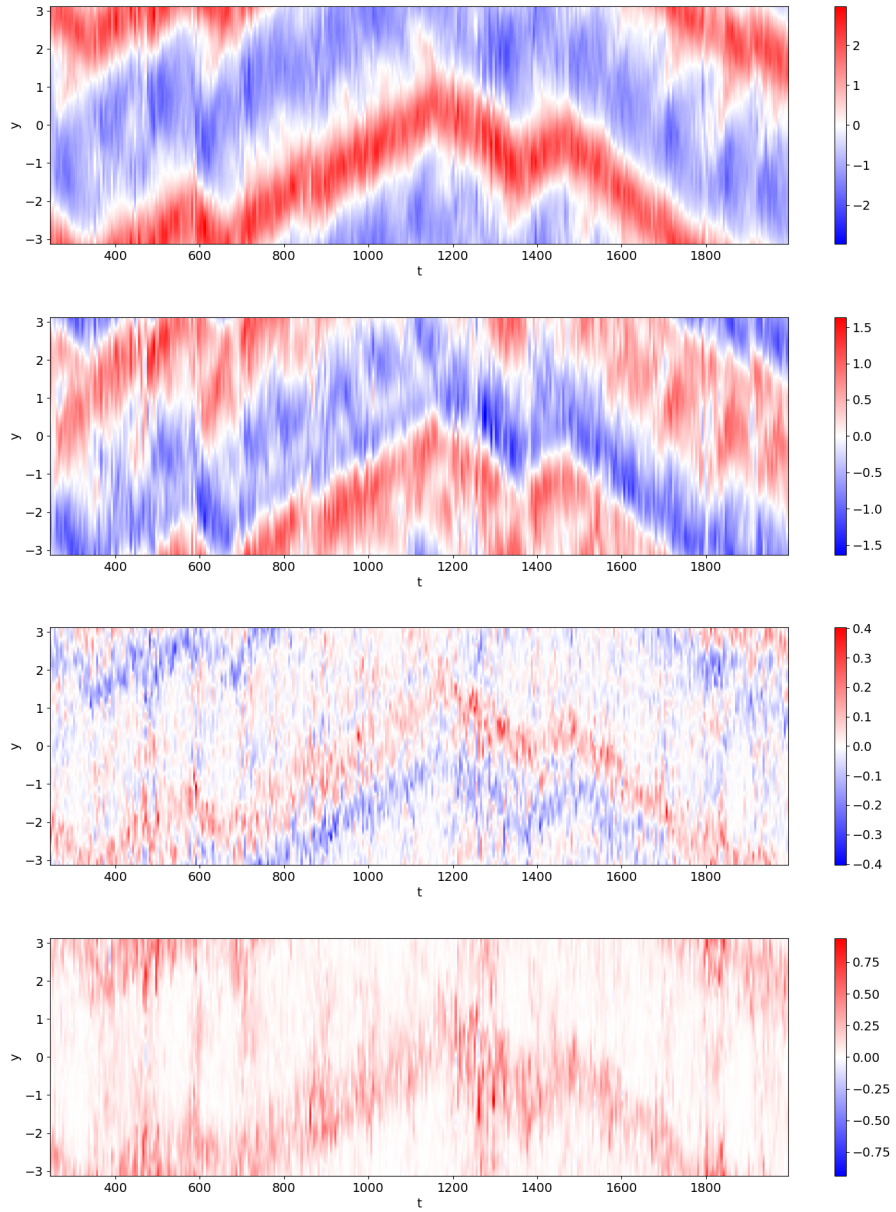

Figure 22: Zonally averaged u_m (top), θ_e (second), q_t (third), vq_t (bottom) as a function of time. $V_r = 1$. (long time)

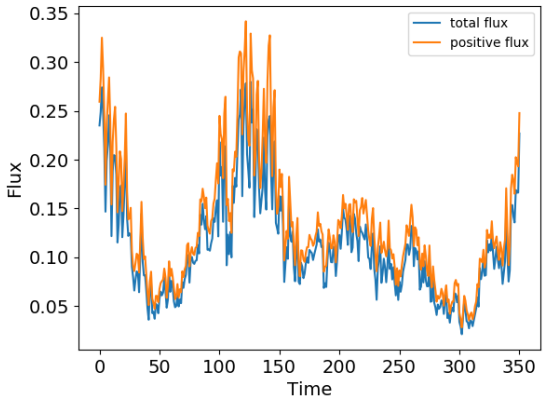

Figure 23: The total meridional flux $< vq_t >$ as a function of time, with $Q_y = -1$.

positive-ness of the total meridional water flux can be observed.

The standard case simulation with $Q_y = -1$ and $V_r = 1$ is presented in figure 23 and the case with no meridional moisture gradient, $Q_y = 0$ in figure 24. The first of these figures shows that the total meridional flux is mostly positive, as can be seen by the two overlapping lines. The second of these figures shows that the total meridional flux is centered around 0, and indicates that the negative flux is not insignificant. As one might expect, the meridional gradient Q_y seems to allow for the meridional water flux to be nonzero and positive, in these simulations.

Figure 25 show the effects of changing the value V_r in the standard case. As the rainfall term acts as a dissipative term, it is expected that the amplitudes of these would decrease with increasing V_r. An interesting feature, however, is that it seems with increased V_r, the positive flux converges to the total flux, indicating that there is less negative flux. Moreover, once V_r is strong enough, the total flux appears to always be positive.

The average percentage of the total flux to the positive flux is computed in table 6,

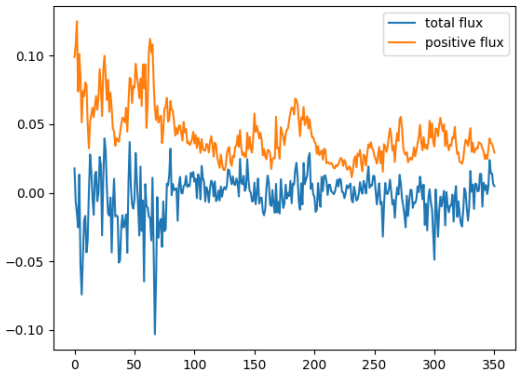

Figure 24: The total meridional flux $< vq_t >$ as a function of time, with $Q_y = 0$. The total meridional flux seems to be centered around zero.

V_r	$< vq_t >_{total} / < vq_t >_{positive}$
0.01	0.161
0.1	0.654
1	0.838
10	0.929

Table 6: The ratio between the total meridional water flux and the positive meridional averaged over time. Larger values of V_r correspond to values closer to 1, meaning that the amount of negative flux is decreasing and that the total flux is composed mostly of the positive flux.

which shows that indeed with increasing V_r the positive flux converges to the total flux.

In the case for large V_r, the importance of Q_y and the positive-ness of the total meridional water flux can be explained by taking the asymptotic limit of $V_r \to \infty$.

From chapter 2, in the asymptotic limit of $V_r \to \infty$ there is the $O(1)$ balance of

$$v_m Q_y - G_M \frac{L_{ds}}{L} w_m = -\frac{V_r}{\Delta z} q_t \tag{3.7}$$

where w_m is the vertical wind at the mid-level. This indicates that for sufficiently large V_r, q_t will appear to be a linear combination of w_m and v_m. By multiplying both side

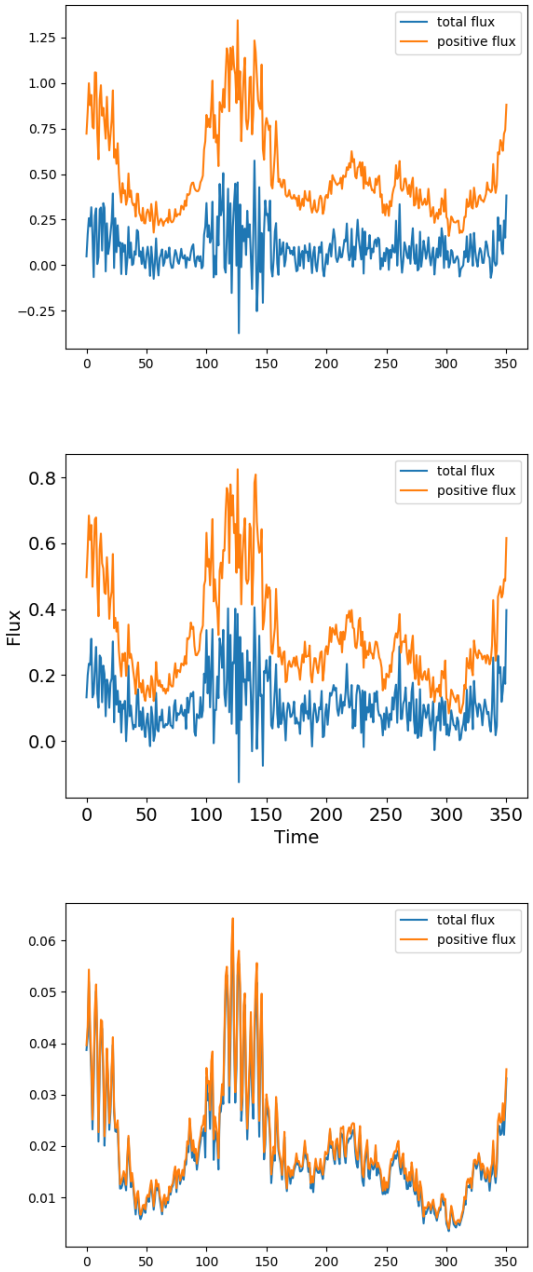

Figure 25: The total meridional flux $< vq_t >$ as a function of time for different V_r. $V_r = 0.01$ (top), $V_r = 0.1$ (middle), $V_r = 10$ (bottom).

by v_m and rearranging some terms to obtain equation 3.8, the meridional water flux can be better understood.

$$v_m q_t = \frac{\Delta z}{V_r}\left(G_M \frac{L_{ds}}{L} w_m v_m - v_m^2 Q_y\right) \tag{3.8}$$

As V_r is increased, from equation 3.7, the $< vq_t >$ begins to resemble a linear combination of $< w_m v_m >$ and $< v_m^2 >$. The second term is positive when $Q_y < 0$, and hence shows that for large enough V_r, the total meridional flux will be positive which is consistent with the observation from figure 25 . Furthermore, we see that when $Q_y = 0$, the contributing term to the meridional flux will only be $< w_m v_m >$ which is not guaranteed to be positive, which is also consistent with figure 24.

Based on some preliminary simulations done with different values of β, it was observed that when the jet was stronger, water would organize near the jet boundary more consistently, whereas for the case of a weak jet which would intermittently show vortical behavior, the organization of water seemed to be more noisier.

3.6 Conclusions

In summary, we have investigated some properties of meridional water transport in a simple model. More specifically, the presence and characteristics of ARs and also the factors influencing the meridional water fluxes were investigated. This was done in a quasi-geostrophic approach by using the saturated PQG model. While this PQG inherits the limitations from two level QG, such as low vertical resolution, and the lack of ability to model fronts due to lack of phase changes, it provides a simple framework which can help understand one aspect of water transport in terms of ARs and meridional fluxes.

Even with this simple model setup, which lacks many physical processes, it was seen that ARs could form and could be identified from the simulations based off the algorithm by Guan and Waliser [2015]. Moreover, it was seen that these ARs could contribute a disproportionate amount of meridional moisture flux compared to its size.

Also, it was observed that in this model varying only the moist parameters, Q_y and V_r, could lead to different behaviors in the total meridional water flux. By using a simple model, these behaviors could be explained in terms of an asymptotic analysis, at least for the case for sufficiently large V_r.

This study suggests that the two level PQG model provides a framework to understand certain aspects of water structures in the atmosphere. In the future, the full version of PQG with phase changes [Smith and Stechmann, 2017] could allow for more insight into the importance of certain physical processes to the structure of water and water fluxes, although most likely at the expense of more complicated analyses.

Appendix A

More Details

A.1 Chapter 1 appendix

A.1.1 Details on $\tilde{q}_t, \tilde{q}_r$

The saturation water vapor takes the value of its background state, so that $q_{vs}^{tot} = \tilde{q}_{vs}$. Taken together, since $\tilde{q}_t = \tilde{q}_v + \tilde{q}_r = q_{vs}^{tot} + \tilde{q}_r$ and the water vapor is always at its saturation value, the anomalies of total water are equal to the anomalies of rain water: $q_t = q_r$. The saturation water vapor $q_{vs}^{tot}(z)$ is taken to be a function of z, since $q_{vs}^{tot}(T^{tot}, p^{tot}) \approx q_{vs}^{tot}(\tilde{T}(z), \tilde{p}(z))$ in this Boussinesq setup where the anomalies T and p are small compared with the background states $\tilde{T}(z)$ and $\tilde{p}(z)$ [e.g., Hernandez-Duenas et al., 2013]. For an environment that remains saturated for all time, the total mixing ratio of water vapor q_v^{tot} is always equal to a prescribed saturation function of altitude $q_{vs}^{tot}(z)$, such that $q_v^{tot} = q_{vs}^{tot}$. Furthermore, the mixing ratio of total water q_t^{tot} is always above saturation, with $q_r^{tot} = q_t^{tot} - q_{vs}^{tot} > 0$. The latter inequality, in turn, implies that the background rain $\tilde{q}_r$ must be sufficiently large to allow for negative anomalies in our simulations (see Section 2.3).

A.1.2 Computation of w

The values for w is obtained by solving the ω equation:

$$-\left(\frac{2}{\Delta z}-\nabla_h^2\left(\frac{L_{ds}}{L}\right)^2\Delta z\right)w=\left[(v_2-v_1)\beta+\left[J(\psi_2,\nabla_h^2\psi_2)-J(\psi_1,\nabla_h^2\psi_1)\right]+\nabla_h^2(v_2u_1-u_2v_1)\right.$$
$$\left.+\kappa_M\nabla^2\psi_1+2U\nabla_h^2\partial_x\left(\psi_2+\psi_1\right)\right] \quad \text{(A.1)}$$

where $J(a,b)$ represents the determinant of the jacobian. The horizontal derivatives are computed spectrally in Fourier space.

A.1.3 Baroclinic instability of the linearized PQG equations in a saturated environment

In the numerical simulations, the initial conditions are a band of linearly unstable eigenmodes. In what follows, these eigenmodes are presented for the PQG equations. The PGQ eigenmodes are similar to the dry QG eigenmodes, but they differ because of the additional moist variable M, as explained below.

The effect of water on the linear stability of the two-level PQG equations can be studied by solving the 'Phillips problem' [Phillips, 1954], which is perhaps the simplest framework to study baroclinic instability on a β-plane. Related formulations of the linear stability problem for the dry QG equations may be found in [Salmon, 1980, Vallis, 2006, Pedlosky, 2013].

From (3.2) written in terms of the streamfunction ψ and M, one can see that (3.2a)-(3.2b) form a closed subsystem for ψ which is mathematically equivalent to the dry Phillips formulation. There is only a one-way coupling with (3.2c), such that ψ influences the dynamics of M but not the other way around. As will be verified below, the presence

of moisture does not introduce new instabilities, but only changes the range of unstable wavelengths and growth rates. The effect of moisture on the growth rate of unstable modes has been examined in previous studies, such as Emanuel et al. [1987], Lapeyre and Held [2004]. The linear instability analysis of the continuously stratified PQG equations without the β-effect (the so-called Eady problem Eady 1949, Pedlosky 2013) has been studied in Wetzel et al. [2017]. Moist baroclinic instability has also been studied in other contexts, such as in, Gall [1976], Thorpe and Emanuel [1985], Whitaker and Davis [1994], Zhang et al. [2007], Booth et al. [2015]. It was observed in Wetzel et al. [2017] that with the continuous PQG in a saturated regime, the ratio between the moist and dry maximum growth rates were comparable to that found in Gall [1976]. However, the wavenumber of the maxmimum growth rate was unchanged in Gall [1976] even with moisture, whereas for Wetzel et al. [2017], the wavenumber increased.

To impose a zonal flow with vertical shear, together with a meridional temperature gradient, the Phillips background streamfunction is chosen at levels $j = 1, 2$ to be $\psi_{j,bg} = U_j y$ with $U_j = (-1)^j U$ and U constant [Haidvogel and Held, 1980, Lapeyre and Held, 2004]. The resulting expressions for θ_e and PV are, respectively, $\theta_{e,bg} = \Theta y = -\frac{L}{L_{ds}}\frac{1}{\Delta z}(2Uy)$ and $PV_{j,bg} = (-1)^j \left(\frac{1}{\Delta z}\frac{L}{L_{ds}}\right)^2 (2Uy)$. For analysis of the saturated environment, we also impose a background water profile $q_{t,bg} = Q_y y$ with Q_y constant. Thus both temperature and water decrease linearly from south to north. From here on, all variables are decomposed into Boussinesq and Phillips background state and anomalies, in which case the equations (3.2) may be written as

$$\frac{\mathrm{D}_1 PV_1}{\mathrm{D}t} - U\partial_x PV_1 + v_1 \partial_y PV_{1,bg} + \beta v_1 = 0 \tag{A.2a}$$

$$\frac{\mathrm{D}_2 PV_2}{\mathrm{D}t} + U\partial_x PV_2 + v_2 \partial_y PV_{2,bg} + \beta v_2 = 0 \tag{A.2b}$$

$$\frac{\mathrm{D}_m M}{\mathrm{D}t} + v_m \partial_y M_{bg} = -\frac{V_r}{\Delta z}\left(M - G_M \theta_e\right) \tag{A.2c}$$

where $M_{bg} = q_{t,bg} + G_M \theta_{e,bg} = (Q_y + G_M \Theta) y$.

The linearized version of (A.2) has constant coefficients U, β, Q_y, G_M, V_r, and thus one may look for exponential solutions $\psi_j = \mathrm{Re}\{\hat{\psi}_j e^{i(kx+ly-\omega t)}\}$ and $M = \mathrm{Re}\{\hat{M} e^{i(kx+ly-\omega t)}\}$, leading to the possible values of ω:

$$\omega^{\pm} = -\frac{k}{k_h^2 + k_{ds}^2}\left\{\beta\left(1 + \frac{k_{ds}^2}{2k_h^2}\right) \mp \frac{k_{ds}^2}{2k_h^2}\left[\beta^2 + \frac{4U^2 k_h^4 (k_h^4 - k_{ds}^4)}{k_{ds}^4}\right]^{1/2}\right\} \tag{A.3a}$$

$$\omega^r = -i\frac{V_r}{\Delta z}, \tag{A.3b}$$

with $k_h = \sqrt{k^2 + l^2}$ and $k_{ds}^2 = 8L^2/L_{ds}^2$.

To simplify the notation, $\hat{\psi}_1, \hat{\psi}_2$ to represent the eigenmodes found from the solution of the two level dry QG linearized instability problem. (For more details, see Vallis [2006], Pedlosky [2013].)

The eigenmode associated with $\omega^{\pm}$ is given by

$$\begin{pmatrix} \hat{\psi}_1 \\ \hat{\psi}_2 \\ -\frac{1}{-i\omega^{\pm} + V_r/\Delta z}\left(\frac{V_r}{\Delta z}\left(G_M \frac{L}{L_{ds}} \frac{\hat{\psi}_2 - \hat{\psi}_1}{\Delta z}\right) - ik\frac{\hat{\psi}_1 + \hat{\psi}_2}{2} M_{bg}\right) \end{pmatrix} \tag{A.4}$$

and that associated with ω^r is given by

$$\begin{pmatrix} 0 \\ 0 \\ 1 \end{pmatrix}. \tag{A.5}$$

The initial conditions for $\hat{\psi}_1, \hat{\psi}_2$ are obtained from a band of these eigenmodes, with uniformly random phase, as in the dry case. For the initial condition of $\hat{M}$, the linear

combination of the $M-$component of $\omega^{\pm} + \alpha\beta\omega^{r}$ is used, with α being the amplitude of the wave from ω^{pm} and β being a random number chosen from a normal distribution.

A.2 Detailed plot

Figure 26 is a more detailed version of figure 18 which shows the distribution of the number of rivers. The darker shade of blue indicates more instances where the same number of rivers were observed.

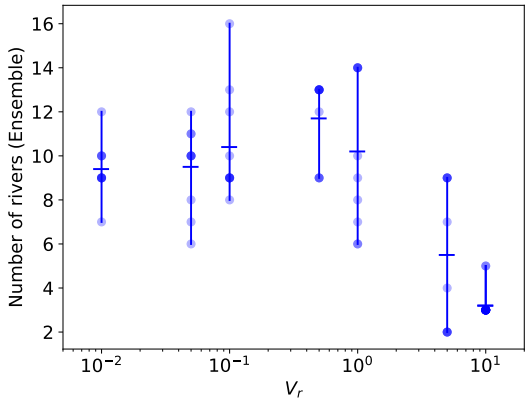

Figure 26: Number of atmospheric rivers observed as a function of the rainfall speed parameter, V_r. $Q_y = 1$. The horizontal bar indicates the average number of rivers from the simulations.

Bibliography

Laurence Armi. Hydraulic control of zonal currents on a β-plane. *Journal of Fluid Mechanics*, 201:357–377, 1989.

Armando Babiano, Claude Basdevant, Bernard Legras, and Robert Sadourny. Vorticity and passive-scalar dynamics in two-dimensional turbulence. *Journal of Fluid Mechanics*, 183:379–397, 1987.

Peter R Bannon. Linear development of quasi-geostrophic baroclinic disturbances with condensational heating. *Journal of the atmospheric sciences*, 43(20):2261–2274, 1986.

JW Bao, SA Michelson, PJ Neiman, FM Ralph, and JM Wilczak. Interpretation of enhanced integrated water vapor bands associated with extratropical cyclones: Their formation and connection to tropical moisture. *Monthly weather review*, 134(4):1063–1080, 2006.

James F Booth, Lorenzo Polvani, Paul A O'Gorman, and Shuguang Wang. Effective stability in a moist baroclinic wave. *Atmospheric Science Letters*, 16(1):56–62, 2015.

Surendra Byna, Michael F Wehner, Kesheng John Wu, et al. Detecting atmospheric rivers in large climate datasets. In *Proceedings of the 2nd international workshop on Petascal data analytics: challenges and opportunities*, pages 7–14. ACM, 2011.

J. G. Charney. The dynamics of long waves in a baroclinic westerly current. *J. Meteorol.*, 4(5):136–162, 1947.

J. G. Charney. On the scale of atmospheric motions. *Geofys. Publ. Oslo*, 17(2):1–17, 1948.

J. G. Charney. Geostrophic turbulence. *J. Atmos. Sci.*, 28(6):1087–1095, 1971.

John YN Cho, Reginald E Newell, and Glen W Sachse. Anomalous scaling of mesoscale tropospheric humidity fluctuations. *Geophysical research letters*, 27(3):377–380, 2000.

Helen F Dacre, Peter A Clark, Oscar Martinez-Alvarado, Marc A Stringer, and David A Lavers. How do atmospheric rivers form? *Bulletin of the American Meteorological Society*, 96(8):1243–1255, 2015.

Michael Dettinger. Climate change, atmospheric rivers, and floods in california–a multimodel analysis of storm frequency and magnitude changes 1. *JAWRA Journal of the American Water Resources Association*, 47(3):514–523, 2011.

Philip G Drazin. *Introduction to hydrodynamic stability*, volume 32. Cambridge university press, 2002.

ERIC T Eady. Long waves and cyclone waves. *Tellus*, 1(3):33–52, 1949.

Kerry A Emanuel, Maurizio Fantini, and Alan J Thorpe. Baroclinic instability in an environment of small stability to slantwise moist convection. part i: Two-dimensional models. *Journal of the atmospheric sciences*, 44(12):1559–1573, 1987.

Lucas Fischer, Christoph Kiemle, and George C Craig. Height-resolved variability of midlatitude tropospheric water vapor measured by an airborne lidar. *Geophysical Research Letters*, 39(6), 2012.

Robert Gall. The effects of released latent heat in growing baroclinic waves. *Journal of the Atmospheric Sciences*, 33(9):1686–1701, 1976.

Yang Gao, Jian Lu, L Ruby Leung, Qing Yang, Samson Hagos, and Yun Qian. Dynamical and thermodynamical modulations on future changes of landfalling atmospheric rivers over western north america. *Geophysical Research Letters*, 42(17):7179–7186, 2015.

Luis Gimeno, Raquel Nieto, Marta Vázquez, and David A Lavers. Atmospheric rivers: A mini-review. *Frontiers in Earth Science*, 2:2, 2014.

Luis Gimeno, Francina Dominguez, Raquel Nieto, Ricardo Trigo, Anita Drumond, Chris JC Reason, Andrea S Taschetto, Alexandre M Ramos, Ramesh Kumar, and Jose Marengo. Major mechanisms of atmospheric moisture transport and their role in extreme precipitation events. *Annual Review of Environment and Resources*, 41: 117–141, 2016.

Bin Guan and Duane E Waliser. Detection of atmospheric rivers: Evaluation and application of an algorithm for global studies. *Journal of Geophysical Research: Atmospheres*, 120(24):12514–12535, 2015.

Dale B Haidvogel and Isaac M Held. Homogeneous quasi-geostrophic turbulence driven by a uniform temperature gradient. *Journal of the Atmospheric Sciences*, 37(12): 2644–2660, 1980.

Isaac M Held and Enda O'Brien. Quasigeostrophic turbulence in a three-layer model: Effects of vertical structure in the mean shear. *Journal of the atmospheric sciences*, 49(19):1861–1870, 1992.

Gerardo Hernandez-Duenas, Andrew J Majda, Leslie M Smith, and Samuel N Stechmann. Minimal models for precipitating turbulent convection. *Journal of Fluid Mechanics*, 717:576–611, 2013.

Gerardo Hernandez-Duenas, Leslie M Smith, and Samuel N Stechmann. Stability and instability criteria for idealized precipitating hydrodynamics. *Journal of the Atmospheric Sciences*, 72(6):2379–2393, 2015.

R.A. Houze. *Cloud dynamics*. Academic Press, San Diego, 1993.

Tianyu Jiang, Katherine J Evans, Yi Deng, and Xiquan Dong. Intermediate frequency atmospheric disturbances: A dynamical bridge connecting western us extreme precipitation with east asian cold surges. *Journal of Geophysical Research: Atmospheres*, 119(7):3723–3735, 2014.

Brian H Kahn and João Teixeira. A global climatology of temperature and water vapor variance scaling from the atmospheric infrared sounder. *Journal of Climate*, 22(20): 5558–5576, 2009.

Brian H Kahn, J Teixeira, EJ Fetzer, Andrew Gettelman, SM Hristova-Veleva, X Huang, AK Kochanski, M Köhler, SK Krueger, R Wood, et al. Temperature and water vapor variance scaling in global models: Comparisons to satellite and aircraft data. *Journal of the Atmospheric Sciences*, 68(9):2156–2168, 2011.

R. Klein and A. Majda. Systematic multiscale models for deep convection on mesoscales. *Theor. Comp. Fluid Dyn.*, 20:525–551, 2006.

Robert H Kraichnan. Inertial ranges in two-dimensional turbulence. *The Physics of Fluids*, 10(7):1417–1423, 1967.

Hsiao-lan Kuo. Dynamic instability of two-dimensional nondivergent flow in a barotropic atmosphere. *Journal of Meteorology*, 6(2):105–122, 1949.

Julien Lambaerts, Guillaume Lapeyre, and Vladimir Zeitlin. Moist versus dry baroclinic instability in a simplified two-layer atmospheric model with condensation and latent heat release. *Journal of the Atmospheric Sciences*, 69(4):1405–1426, 2012.

G Lapeyre and IM Held. The role of moisture in the dynamics and energetics of turbulent baroclinic eddies. *Journal of the atmospheric sciences*, 61(14):1693–1710, 2004.

G Lapeyre, BL Hua, and P Klein. Dynamics of the orientation of active and passive scalars in two-dimensional turbulence. *Physics of Fluids*, 13(1):251–264, 2001.

Vitaly D Larichev and Isaac M Held. Eddy amplitudes and fluxes in a homogeneous model of fully developed baroclinic instability. *Journal of physical oceanography*, 25 (10):2285–2297, 1995.

David A Lavers, Richard P Allan, Eric F Wood, Gabriele Villarini, David J Brayshaw, and Andrew J Wade. Winter floods in britain are connected to atmospheric rivers. *Geophysical Research Letters*, 38(23), 2011.

David A Lavers, Gabriele Villarini, Richard P Allan, Eric F Wood, and Andrew J Wade. The detection of atmospheric rivers in atmospheric reanalyses and their links to british winter floods and the large-scale climatic circulation. *Journal of Geophysical Research: Atmospheres*, 117(D20), 2012.

Mankin Mak. On moist quasi-geostrophic baroclinic instability. *Journal of the Atmospheric Sciences*, 39(9):2028–2037, 1982.

ME Maltrud and GK Vallis. Energy spectra and coherent structures in forced two-dimensional and beta-plane turbulence. *Journal of Fluid Mechanics*, 228:321–342, 1991.

Juan Pedro Mellado. Cloud-top entrainment in stratocumulus clouds. *Annual Review of Fluid Mechanics*, 49:145–169, 2017.

Joy M Monteiro and Jai Sukhatme. Quasi-geostrophic dynamics in the presence of moisture gradients. *Quarterly Journal of the Royal Meteorological Society*, 142(694): 187–195, 2016.

H. Morrison and W. W. Grabowski. Modeling supersaturation and subgrid-scale mixing with two-moment bulk warm microphysics. *J. Atmos. Sci.*, 65(3):792–812, 2008.

GD Nastrom, WH Jasperson, and KS Gage. Horizontal spectra of atmospheric tracers measured during the global atmospheric sampling program. *Journal of Geophysical Research: Atmospheres*, 91(D12):13201–13209, 1986.

Munir A Nayak, Gabriele Villarini, and David A Lavers. On the skill of numerical weather prediction models to forecast atmospheric rivers over the central united states. *Geophysical Research Letters*, 41(12):4354–4362, 2014.

Paul J Neiman, F Martin Ralph, Gary A Wick, Jessica D Lundquist, and Michael D

Dettinger. Meteorological characteristics and overland precipitation impacts of atmospheric rivers affecting the west coast of north america based on eight years of ssm/i satellite observations. *Journal of Hydrometeorology*, 9(1):22–47, 2008.

Paul J Neiman, Allen B White, F Martin Ralph, Daniel J Gottas, and Seth I Gutman. A water vapour flux tool for precipitation forecasting. In *Proceedings of the Institution of Civil Engineers-Water Management*, volume 162, pages 83–94. Thomas Telford Ltd, 2009.

Joseph Pedlosky. *Geophysical fluid dynamics*. Springer Science & Business Media, 2013.

Norman A Phillips. A simple three-dimensional model for the study of large-scale extratropical flow patterns. *Journal of Meteorology*, 8(6):381–394, 1951.

Norman A Phillips. Energy transformations and meridional circulations associated with simple baroclinic waves in a two-level, quasi-geostrophic model. *Tellus*, 6(3):274–286, 1954.

Kyle G Pressel and William D Collins. First-order structure function analysis of statistical scale invariance in the airs-observed water vapor field. *Journal of Climate*, 25 (16):5538–5555, 2012.

Di Qi and Andrew J Majda. Low-dimensional reduced-order models for statistical response and uncertainty quantification: Two-layer baroclinic turbulence. *Journal of the Atmospheric Sciences*, 73(12):4609–4639, 2016.

F Martin Ralph, Paul J Neiman, and Gary A Wick. Satellite and caljet aircraft observations of atmospheric rivers over the eastern north pacific ocean during the winter of 1997/98. *Monthly Weather Review*, 132(7):1721–1745, 2004.

F Martin Ralph, Michael D Dettinger, Mary M Cairns, Thomas J Galarneau, and John Eylander. Defining atmospheric river: How the glossary of meteorology helped resolve a debate. *Bulletin of the American Meteorological Society*, 99(4):837–839, 2018.

F Martin Ralph, Jonathan J Rutz, Jason M Cordeira, Michael Dettinger, Michael Anderson, David Reynolds, Lawrence J Schick, and Chris Smallcomb. A scale to characterize the strength and impacts of atmospheric rivers. *Bulletin of the American Meteorological Society*, (2019), 2019.

FM Ralph and MD Dettinger. Storms, floods, and the science of atmospheric rivers. *Eos, Transactions American Geophysical Union*, 92(32):265–266, 2011.

FM Ralph, T Coleman, PJ Neiman, RJ Zamora, and MD Dettinger. Observed impacts of duration and seasonality of atmospheric-river landfalls on soil moisture and runoff in coastal northern california. *Journal of Hydrometeorology*, 14(2):443–459, 2013.

Peter B Rhines. Geostrophic turbulence. *Annual Review of Fluid Mechanics*, 11(1): 401–441, 1979.

R.R. Rogers and M.K. Yau. *A short course in cloud physics*. Butterworth–Heinemann, Burlington, 1989.

Jonathan J Rutz, W James Steenburgh, and F Martin Ralph. Climatological characteristics of atmospheric rivers and their inland penetration over the western united states. *Monthly Weather Review*, 142(2):905–921, 2014.

Rick Salmon. Baroclinic instability and geostrophic turbulence. *Geophysical & Astrophysical Fluid Dynamics*, 15(1):167–211, 1980.

Rick Salmon. *Lectures on geophysical fluid dynamics*. Oxford University Press, 1998.

Vera Schemann, Bjorn Stevens, Verena Grützun, and Johannes Quaas. Scale dependency of total water variance and its implication for cloud parameterizations. *Journal of the Atmospheric Sciences*, 70(11):3615–3630, 2013.

Barrett L Smith, Sandra E Yuter, Paul J Neiman, and DE Kingsmill. Water vapor fluxes and orographic precipitation over northern california associated with a landfalling atmospheric river. *Monthly Weather Review*, 138(1):74–100, 2010.

K Shafer Smith and Geoffrey K Vallis. The scales and equilibration of midocean eddies: Freely evolving flow. *Journal of Physical Oceanography*, 31(2):554–571, 2001.

KS Smith, G Boccaletti, CC Henning, I Marinov, CY Tam, IM Held, and GK Vallis. Turbulent diffusion in the geostrophic inverse cascade. *Journal of Fluid Mechanics*, 469:13–48, 2002.

Leslie M Smith and Samuel N Stechmann. Precipitating quasi-geostrophic equations and potential vorticity inversion with phase changes. *Journal of the Atmospheric Sciences*, (2017), 2017.

K Spyksma and P Bartello. Small-scale moist turbulence in numerically generated convective clouds. *Journal of the Atmospheric Sciences*, 65(6):1967–1978, 2008.

Jai Sukhatme, Andrew J Majda, and Leslie M Smith. Two-dimensional moist stratified turbulence and the emergence of vertically sheared horizontal flows. *Physics of Fluids*, 24(3):036602, 2012.

AJ Thorpe and KA Emanuel. Frontogenesis in the presence of small stability to slantwise convection. *Journal of the atmospheric sciences*, 42(17):1809–1824, 1985.

Geoffrey K Vallis. Atmospheric and oceanic fluid dynamics. *Atmospheric and Oceanic Fluid Dynamics, by Geoffrey K. Vallis, pp. 770. Cambridge University Press, November 2006. ISBN-10: 0521849691. ISBN-13: 9780521849692*, page 770, 2006.

Duane E Waliser, Mitchell W Moncrieff, David Burridge, Andreas H Fink, Dave Gochis, BN Goswami, Bin Guan, Patrick Harr, Julian Heming, Huang-Hsuing Hsu, et al. The year of tropical convection (may 2008–april 2010): Climate variability and weather highlights. *Bulletin of the American Meteorological Society*, 93(8):1189–1218, 2012.

Alfredo N Wetzel, Leslie M Smith, and Samuel N Stechmann. Moisture transport due to baroclinic waves: Linear analysis of precipitating quasi-geostrophic dynamics. *Mathematics of Climate and Weather Forecasting*, 3(1):28–50, 2017.

Jeffrey S Whitaker and Christopher A Davis. Cyclogenesis in a saturated environment. *Journal of the atmospheric sciences*, 51(6):889–908, 1994.

Gary A Wick, Paul J Neiman, and F Martin Ralph. Description and validation of an automated objective technique for identification and characterization of the integrated

water vapor signature of atmospheric rivers. *IEEE Transactions on Geoscience and Remote Sensing*, 51(4):2166–2176, 2013.

Fuqing Zhang, Naifang Bei, Richard Rotunno, Chris Snyder, and Craig C Epifanio. Mesoscale predictability of moist baroclinic waves: Convection-permitting experiments and multistage error growth dynamics. *Journal of the Atmospheric Sciences*, 64(10):3579–3594, 2007.

Yong Zhu and Reginald E Newell. A proposed algorithm for moisture fluxes from atmospheric rivers. *Monthly weather review*, 126(3):725–735.